IEEE Access
Multidisciplinary ⋮ Rapid Review ⋮ Open Access Journal

Received 26 November 2024, accepted 20 January 2025, date of publication 27 January 2025, date of current version 3 February 2025.

Digital Object Identifier 10.1109/ACCESS.2025.3535093

TOPICAL REVIEW

C_n^2 Modeling for Free-Space Optical Communications: A Review

FLORIAN QUATRESOOZ AND CLAUDE OESTGES, (Fellow, IEEE)
ICTEAM, Université catholique de Louvain (UCLouvain), 1348 Louvain-la-Neuve, Belgium
Corresponding author: Florian Quatresooz (florian.quatresooz@uclouvain.be)

ABSTRACT Atmospheric turbulence influence on optical wave propagation, referred to as optical turbulence, has long been studied for astronomical applications and is now being addressed for free-space optical communication links between ground and satellites. While challenges overlap, models developed for astronomical applications are not fully transferable to optical communications. This paper provides a literature review of optical turbulence models, i.e., models giving vertical profiles of the refractive index structure parameter C_n^2, highlighting differences between astronomical and optical communication sites. It presents different classifications of available C_n^2 models, based on the atmospheric layer they target and their necessary input parameters. Boundary layer C_n^2 models are also addressed, and recent machine learning approaches for C_n^2 modeling are discussed. Additionally, commonly used metrics for comparing C_n^2 profiles are introduced. Therefore, this work provides important insights into optical turbulence model selection, enabling accurate site characterization and informed optical terminal design.

INDEX TERMS Atmospheric turbulence modeling, free-space optical communications, optical turbulence.

I. INTRODUCTION

Free-space optical communications (FSOC) between the ground and satellites promise to enhance connectivity, boost achievable data rates and offer viable alternatives to fiber-optic networks. As the technological revolution is ongoing and optical ground stations (OGS) are being installed and commissioned worldwide, challenges associated with the propagation of light through Earth's atmosphere remain to be addressed.

In particular, the impact of atmospheric turbulence on optical waves, referred to as optical turbulence (OT), is a major challenge. Accounting for OT is essential to ensure the reliability of future FSOC networks, giving them the capability and robustness to operate in various atmospheric and environmental conditions.

The study of OT has been conducted for several decades at astronomical sites. However, future OGS locations face distinct OT conditions compared to astronomical observatories for two main reasons: (i) FSOC will take place in or near urban areas, where communication demand is highest, rather than in remote, high-altitude locations; (ii) FSOC require daytime operations, unlike traditional nighttime astronomical observations. As a result, stronger OT conditions are expected, primarily due to the enhanced boundary layer contribution associated with low-altitude locations and daytime operation [1].

OT is commonly characterized by the refractive index structure parameter, C_n^2. This statistical quantity is related to Kolmogorov theory of turbulence [2] and varies with altitude, geographic location, seasons and time of day. Altitude variations of C_n^2 lead to the concept of C_n^2 profile, a key parameter from which OT-integrated quantities (e.g., coherence length, seeing, scintillation index, etc.) and FSOC performance metrics are derived [3], [4].

Recent measurement campaigns confirm that C_n^2 profiles at potential FSOC sites exhibit distinctive features compared to those at astronomical locations [5], [6]. These findings highlight the need for further research in the field of C_n^2 profile modeling to achieve accurate characterization and reliable predictions of C_n^2 in diverse locations [7].

This paper provides a timely review of C_n^2 models available in the literature. In an attempt to classify these models, this paper emphasizes their origins to ensure that their original

The associate editor coordinating the review of this manuscript and approving it for publication was Paulo Mendes.

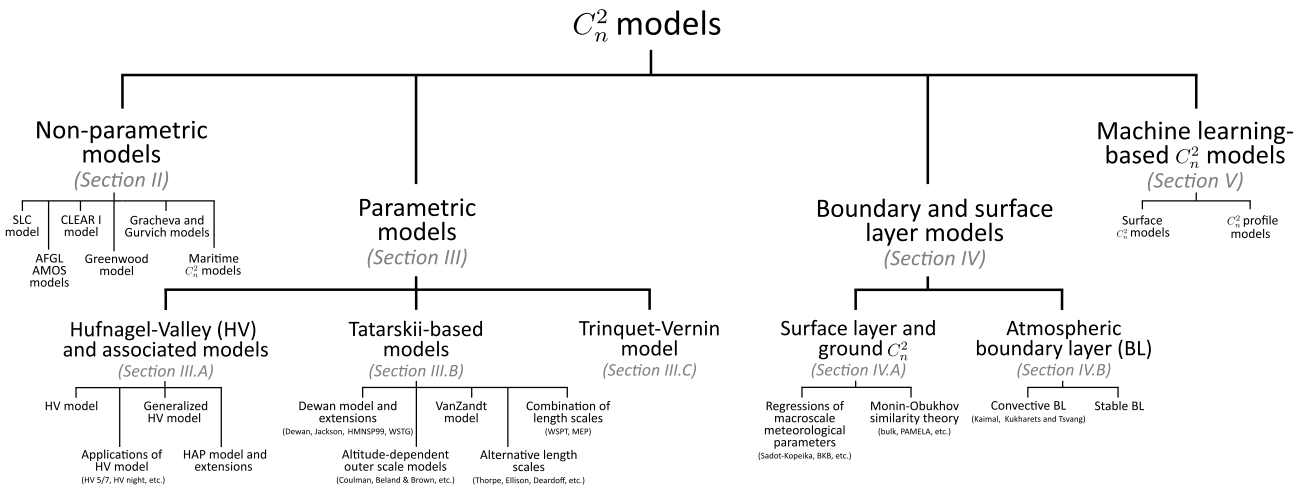

FIGURE 1. Paper structure and presented classification of C_n^2 models.

areas of application remain clear. This is especially important for C_n^2 models developed for specific locations and seasons, as their application to other places and times must only be conducted with proper validation.

Building upon prior literature reviews of C_n^2 models [8], [9], [10], [11], this work makes the following contributions:

- It provides an essential and comprehensive update, as most existing reviews are outdated and focused primarily on astronomical applications.
- It offers a clear classification of C_n^2 models, highlighting their motivations and limitations.
- It also focuses on C_n^2 modeling in the boundary layer, including diurnal variation, essential for OGS sites.
- It presents machine learning (ML)-based C_n^2 models, which have recently gained attraction in the literature.

Hence, this paper provides the FSOC community with precious insights for selecting and applying accurate C_n^2 models, yielding realistic information about OT that can be exploited for site selection and characterization, optical terminal design, and FSOC network operation.

A. PAPER STRUCTURE

The structure of the paper, with the presented classification of C_n^2 models, is shown in Figure 1.

Sections II and III detail non-parametric and parametric C_n^2 models, mostly adapted for modeling the free atmosphere (FA), i.e., the part of the atmosphere where the ground influence is marginal, as opposed to the boundary layer (BL). Following the terminology in [8] and [9], parametric models refer to models using macroscale meteorological quantities as inputs (e.g., pressure, temperature, humidity, etc.) to model C_n^2 profiles. Such models are of particular interest as they can be adapted to local conditions. On the contrary, non-parametric models only give access to C_n^2 profiles as a function of altitude, derived from empirical observations.

Then, Section IV focuses on boundary layer C_n^2 models, whereas Section V presents the recent developments in machine learning-based models. Finally, Section VI concludes the review and provides our views on C_n^2 modeling for FSOC. In addition, Appendix A discusses relevant metrics used to validate and compare C_n^2 models.

B. NOTATIONS

The following notations are used for the meteorological quantities throughout this paper: pressure p in pascal [Pa] or hectopascal [hPa], temperature T in kelvin [K], specific humidity q in [kg/kg]. The wind horizontal components in x and y directions are denoted u and v, with $u_L = \sqrt{u^2+v^2}$ the total wind speed. The potential temperature $\theta = T\left(\frac{p_0}{p}\right)^{R/c_p}$ in [K] is also exploited below and corresponds to the temperature that an air parcel initially at temperature T and pressure p would reach if moved adiabatically to a standard reference pressure p_0 (usually, $p_0 = 1000$ hPa). It involves the gas constant of air R and the specific heat capacity at constant pressure c_p.

Most of the C_n^2 models presented use the variable z as the altitude in [m], defined as the altitude above the surface. However, some models in Sections II and III consider z as the altitude above mean sea level. In this case, it is specified with the model.

II. NON-PARAMETRIC MODELS

Non-parametric models describe C_n^2 profiles solely as a function of altitude, i.e., $C_n^2(z) = f(z)$, where $f(.)$ is a generic function depending on the models. They are simple to use and are typically derived from the averaging of measurement sets collected at a specific location during a particular season. As such, they are considered as empirical models, dependent on both location and season. Moreover, due to this averaging, these models cannot capture the stratification in C_n^2 profiles or account for temporal variations. Nevertheless, despite these limitations, their application to obtain median or averaged profiles and to compare different sites still makes them

relevant [8, p. 171]. Several C_n^2 profiles presented in this section are depicted in Figure 2 to facilitate their comparison.

A. SLC MODEL

The Submarine Laser Communication (SLC) model is an empirical profile derived from multiple measurements (e.g., scintillation, acoustic soundings, microthermal probes) above the Air Force Maui Optical Station (AMOS), Haleakalā, Hawaii [12]. It was initially a nighttime model, but a daytime extension has been developed [9]. Using z as the altitude above the ground (the ground altitude is 3.038 km at Mount Haleakalā) expressed in meters, the nighttime SLC model is given by [9, p. 218], [12, p. 121]

$$C_n^2(z) = \begin{cases} 8.40 \times 10^{-15} & \text{for } z \leq 18.5 \text{ m} \\ 2.87 \times 10^{-12}\, z^{-2} & \text{for } 18.5 < z \leq 110 \text{ m} \\ 2.50 \times 10^{-16} & \text{for } 110 < z \leq 1500 \text{ m} \\ 8.87 \times 10^{-7}\, z^{-3} & \text{for } 1500 < z \leq 7200 \text{ m} \\ 2.00 \times 10^{-16}\, z^{-0.5} & \text{for } 7200 < z \leq 20000 \text{ m}. \end{cases}$$

The daytime SLC model only differs for the altitudes below 1500 m, and is obtained from

$$C_n^2(z) = \begin{cases} 1.70 \times 10^{-14} & \text{for } z \leq 18.5 \text{ m} \\ 3.13 \times 10^{-13}\, z^{-1} & \text{for } 18.5 < z \leq 240 \text{ m} \\ 1.30 \times 10^{-15} & \text{for } 240 < z \leq 880 \text{ m} \\ 8.87 \times 10^{-7}\, z^{-3} & \text{for } 880 < z \leq 7200 \text{ m} \\ 2.00 \times 10^{-16}\, z^{-0.5} & \text{for } 7200 < z \leq 20000 \text{ m}. \end{cases}$$

Comments about the model derivation and its limitations can be found in [9, p. 218]. Slightly different coefficients for the daytime model can be found in [13, p. 61], [14].

B. AFGL AMOS MODELS

Based on more high-resolution balloon measurements above Mount Haleakalā, the nighttime SLC model has been refined, leading to the Air Force Geophysical Laboratory (AFGL) AMOS model [9, p. 219], [8, p. 173]. As the SLC models, it is based on piecewise fitting of the measured profiles. The nighttime AFGL AMOS model is given by [9, p. 219]

$$\log_{10}(C_n^2(z)) = -12.412 - 0.4713\, z - 0.0906\, z^2,$$

for 3.052 km $< z \leq$ 5.2 km and

$$\log_{10}(C_n^2(z)) = -17.1273 - 0.0301\, z - 0.0010\, z^2 + 0.5061\, \mathrm{e}^{-0.5\left(\frac{z-15.0866}{3.2977}\right)^2},$$

for 5.2 km $< z \leq$ 30 km, with z *the altitude above the mean sea level expressed in kilometres*. The differences between the nighttime SLC and AFGL AMOS models are discussed in [9, p. 219]. A daytime version of the model is presented in [8, p. 173], with

$$\log_{10}(C_n^2(z)) = 0.0482 - 2.3416\, z - 0.7211\, z^2,$$

for $z <$ 3.54 km,

$$\log_{10}(C_n^2(z)) = -17.4778 + 0.0320\, z + 0.0078\, z^2 + 1.5066\, \mathrm{e}^{-0.5\left(\frac{z-4.4603}{0.0968}\right)^2},$$

for 3.54 $\leq z <$ 5.1 km, and

$$\log_{10}(C_n^2(z)) = -16.5589 - 0.1424\, z + 0.0030\, z^2 + 1.5694\, \mathrm{e}^{-0.5\left(\frac{z-16.6300}{4.8757}\right)^2},$$

for $z \geq$ 5.1 km. A sunrise version is also available [8, p. 173]:

$$\log_{10}(C_n^2(z)) = -14.0245 - 0.4809\, z - 0.0144\, z^2,$$

for $z <$ 5.78 km and

$$\log_{10}(C_n^2(z)) = -16.7545 + 0.0259\, z - 0.0022\, z^2 - 0.6693\, \mathrm{e}^{-0.5\left(\frac{z-7.0330}{2.8558}\right)^2},$$

for $z \geq$ 5.78 km.

C. CLEAR I MODEL

Using a similar approach as the AFGL AMOS models, the Critical Laser Enhancing Atmospheric Research (CLEAR) I model has been derived from measurements in the Tularosa Basin, New Mexico, during the summer [9, p. 220], [15]. The CLEAR I nighttime model is given by

$$\log_{10}(C_n^2(z)) = -10.7025 - 4.3507\, z + 0.8141\, z^2,$$

for 1.23 $< z \leq$ 2.13 km,

$$\log_{10}(C_n^2(z)) = -16.2897 + 0.0335\, z - 0.0134\, z^2,$$

for 2.13 $< z \leq$ 10.34 km, and

$$\log_{10}(C_n^2(z)) = -17.0577 - 0.0449\, z - 0.0005\, z^2 + 0.6181\, \mathrm{e}^{-0.5\left(\frac{z-15.5617}{3.4666}\right)^2},$$

for 10.34 $< z \leq$ 30 km, with z *the altitude above mean sea level in km* (the ground altitude is 1.216 km in the location where the model was obtained). A revision of the CLEAR I model can be found in [15, p. 35].

D. GREENWOOD MODEL

Another model based on nighttime C_n^2 measurements at AMOS is the Greenwood model [16] [13, p. 62]

$$C_n^2(z) = \left(2.2 \times 10^{-13}\, (z+10)^{-1.3} + 4.3 \times 10^{-17}\right) \mathrm{e}^{-\frac{z}{4000}},$$

where z is the altitude above the ground (in meters). The model has initially been presented with a dependency to the zenith angle ϑ, substituting the altitude z by $l\cos(\vartheta)$, with l the distance from the telescope aperture [13, p. 61]. It is considered as a "good seeing" model in [8, p. 179], while its "poor seeing" version is given by

$$C_n^2(z) = \left(2.2 \times 10^{-12}\, (z+10)^{-1.3} + 7 \times 10^{-16}\right) \mathrm{e}^{-\frac{z}{2000}}.$$

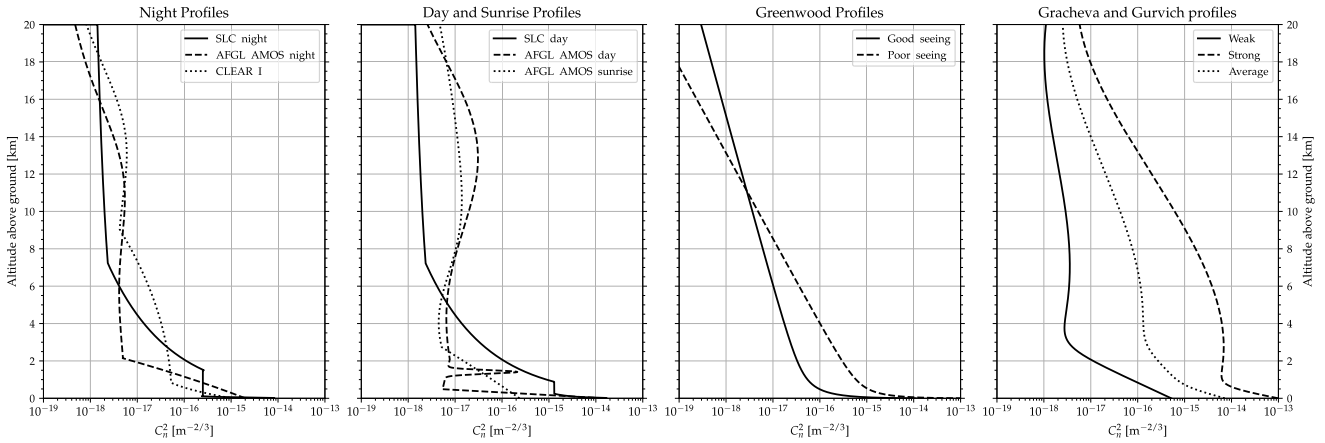

FIGURE 2. Representations of main non-parametric C_n^2 models, expressed in altitude above ground (the ground altitude at locations where the models were obtained may be different, as detailed in the text for each model).

E. GRACHEVA AND GURVICH MODELS

Gracheva and Gurvich models, presented in [10] and [17], provide some fitting of the logarithm in base 10 of the C_n^2 profile based on numerous experimental measurements. A separation between weak and strong turbulence conditions is made, leading to the weak turbulence model

$$\log_{10}\left(C_{n,\min}^2(z) - 5.19\times10^{-16}\times10^{-0.00086\,z}\right) = -18.34 + 2.9\times10^{-4}\,z - 2.84\times10^{-8}\,z^2 + 7.43\times10^{-13}\,z^3,$$

and the strong turbulence model

$$\log_{10}\left(C_{n,\max}^2(z) - 9.5\times10^{-14}\times10^{-0.00209\,z}\right) = -14.39 + 1.7\times10^{-4}\,z - 3.48\times10^{-8}\,z^2 + 9.59\times10^{-13}\,z^3,$$

with z the altitude above ground, in meters. A model for average atmospheric conditions is derived from the average of the weak and strong turbulence models, i.e.,

$$\log_{10}\left(C_{n,\mathrm{av}}^2(z)\right) = \frac{1}{2}\left[\log_{10}\left(C_{n,\min}^2(z)\right) + \log_{10}\left(C_{n,\max}^2(z)\right)\right].$$

F. MARITIME C_N^2 MODELS

The maritime C_n^2 models, presented in [18] and inspired from the Hufnagel-Valley model (see Section III-A1), aim at providing a standard profiles for maritime conditions. They have been derived from a collection of measurements near or over the ocean, and use the generic form

$$C_n^2(z) = c_1 + c_2\,\mathrm{e}^{-z/c_3} + c_4\,\mathrm{e}^{-z/c_5}. \tag{1}$$

The altitude z is in meters and spans from 0 to 6000 m. The values of the different coefficients c in (1) depend on the considered cases (worst, median, or best conditions) and are given in Table 1.

TABLE 1. Coefficients in maritime C_n^2 models in (1) [18].

Cases	"Best"	"Median"	"Worst"
c_1 [m$^{-2/3}$]	9.8286×10^{-18}	9.8583×10^{-18}	9.2002×10^{-18}
c_2 [m$^{-2/3}$]	7.1609×10^{-17}	4.9877×10^{-16}	9.4387×10^{-15}
c_3 [m]	100	300	800
c_4 [m$^{-2/3}$]	1.9521×10^{-17}	2.9228×10^{-16}	6.7328×10^{-16}
c_5 [m]	1500	1200	1000

III. PARAMETRIC MODELS

Unlike non-parametric models, parametric models of C_n^2 profiles account for location and seasonal dependencies. These models are based on the general expression $C_n^2(z) = f(z,t,p,T,\dots)$, where C_n^2 is related to macroscale meteorological parameters (e.g., pressure p, temperature T), time of day t, and other factors. Parametric models can have a theoretical basis, such as Tatarskii-based models presented in Section III-B, or an empirical origin, like the Hufnagel-Valley (HV) model or the Trinquet-Vernin (TV) model given in Sections III-A and III-C.

A. HUFNAGEL-VALLEY MODEL AND ASSOCIATED MODELS

The HV model, along with its commonly used extensions in the literature, are presented in this section. These are simple models involving few parameters, and when the values of these parameters are known, they can be treated as non-parametric models (e.g., the HV-5/7 model described in Section III-A2).

1) HUFNAGEL-VALLEY MODEL

Early C_n^2 models, referenced in [8, p. 170], proposed an exponential decrease of C_n^2 with altitude. Later observations revealed that this average exponential decrease was primarily valid in the troposphere, and that the models needed to be extended to account for contributions from the tropopause [19]. These considerations are apparent in the Hufnagel model, which was derived from stellar observations

and thermosonde measurements [20]. Its simplest form is given by [21]

$$C_n^2(z) = 2.7 \times 10^{-16} \mathrm{e}^{-\frac{z}{1500}} + 8.2 \times 10^{-56} w^2 z^{10} \mathrm{e}^{-\frac{z}{1000}}, \tag{2}$$

where z *is the altitude in meters above sea level*, and w is the Root-Mean-Square (RMS) wind speed, averaged from 5 km to 20 km of altitude. It is only valid above the first strong inversion layer, setting its limits from 3 km to 24 km of altitude [8, p. 174]. Interestingly, (2) contains two terms, the first one being an exponential decrease associated with the troposphere, and the second one representing a bump in the C_n^2 profile at the tropopause and its stratospheric decrease. The origin of the coefficient 2.7 in front of the exponential decrease is briefly detailed in [8, p. 175], while the RMS wind speed can be computed from the wind speed profile $u_L(z)$, with

$$w^2 = \frac{1}{15000} \int_{5000}^{20000} u_L^2(z)\, \mathrm{d}z. \tag{3}$$

This explains why the Hufnagel model belongs to the parametric models, as it depends on local meteorological quantities (wind speed profile) through the parameter w.

In [21], a value of 27 m/s is suggested for the parameter w in order to obtain a fixed model. Random models can also be generated by considering w as a Gaussian random variable, having a mean value of 27 m/s and a standard deviation of 9 m/s. This particular value of 27 m/s led to the rewriting of the Hufnagel model with [4, p. 481]

$$C_n^2(z) = 2.7 \times 10^{-16} \mathrm{e}^{-\frac{z}{1500}} + 0.00594 \left(\frac{w}{27}\right)^2 \left(\frac{z}{10^5}\right)^{10} \mathrm{e}^{-\frac{z}{1000}}.$$

Later, according to [8, p. 175] and [9, p. 222], Ulrich [22] extended the Hufnagel model to include a boundary layer term, following a suggestion of Valley [23]. This led to the well-known HV model, given by

$$C_n^2(z) = A\, \mathrm{e}^{-\frac{z}{100}} + 2.7 \times 10^{-16} \mathrm{e}^{-\frac{z}{1500}} + 0.00594 \left(\frac{w}{27}\right)^2 \left(\frac{z}{10^5}\right)^{10} \mathrm{e}^{-\frac{z}{1000}}. \tag{4}$$

In (4), the BL term is assumed to be exponential and involves the parameter A, associated to the ground C_n^2 value [$\mathrm{m}^{-2/3}$]. As a result, the HV model has two parameters, A and w, that can be adjusted to model C_n^2 variations at high altitudes and near the ground. This offers a certain freedom to adapt the model to different geographical locations [24], even though it remains mostly suited for mid-latitude regions [8, p. 175]. The International Telecommunication Union (ITU) Recommendation P.1621-2 [25] suggests using the HV model to calculate C_n^2 profiles for frequencies between 20 THz and 375 THz. Figure 3 shows C_n^2 profiles obtained using the HV model with different parameters A and w. These profiles are compared with the HV-5/7 model ($A = 1.7 \times 10^{-14}$ $\mathrm{m}^{-2/3}$ and $w = 21$ m/s), described below. In the legend, parameters not specified correspond to those of the HV-5/7 model. The figure highlights that the parameter A primarily affects C_n^2 in the BL, while w influences C_n^2 in the tropopause and stratosphere.

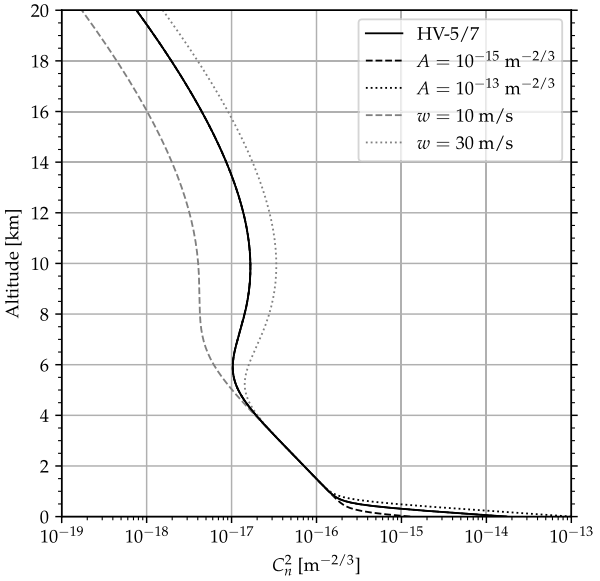

FIGURE 3. Hufnagel-Valley model variations with *w* and *A* parameters (adapted from [26]).

2) APPLICATIONS OF HUFNAGEL-VALLEY MODEL

The adaptability of the HV model, along with its simplicity, explain its widespread use for practical and theoretical studies. Some of them are detailed in this section.

a: HUFNAGEL-VALLEY 5/7 MODEL

The most well-known parametrization of the HV model is the HV 5/7 model, denoted HV-5/7. The parameters are: $A = 1.7 \times 10^{-14}$ $\mathrm{m}^{-2/3}$ and $w = 21$ m/s [9, p. 222].

The HV-5/7 model is named after the values of some OT integrated parameters that it yields, namely the coherence length r_0 (Fried parameter) and the isoplanatic angle θ_0, defined by [27]

$$r_0 = \left(0.423\, k^2 \sec(\vartheta) \int_0^\infty C_n^2(z)\, \mathrm{d}z\right)^{-3/5} \tag{5}$$

$$\theta_0 = \left(2.914\, k^2 (\sec(\vartheta))^{8/3} \int_0^\infty C_n^2(z) z^{5/3}\, \mathrm{d}z\right)^{-3/5}, \tag{6}$$

with $k = 2\pi/\lambda$ (λ is the wavelength) and ϑ the zenith angle. Indeed, vertical integration of the HV-5/7 model using (5) and (6) gives a coherence length of 5 cm and an isoplanatic angle of 7 μrad, assuming a wavelength of 500 nm.

b: HUFNAGEL-VALLEY NIGHT MODEL

A parameterization of the HV model compatible with observations at AMOS is presented in [14], that is,

$$C_n^2(z) = 1.90 \times 10^{-15}\, \mathrm{e}^{-\frac{z}{100}} + 3.02 \times 10^{-17} \mathrm{e}^{-\frac{z}{1500}} + 8.16 \times 10^{-54}\, z^{10}\, \mathrm{e}^{-\frac{z}{1000}},$$

with z the altitude in meters. This modified version of the HV model yields a coherence length of 20 cm and an isoplanatic angle of 20 μrad, for a wavelength of 550 nm, at zenith.

c: MODELS OF WIND SPEED PROFILE

The determination of the w parameter can be achieved using (3), which requires the knowledge of the wind speed profile. In cases where this profile cannot be observed, the Bufton wind model is often used in the literature. It is inspired by simultaneous measurements of C_n^2, temperature, and wind velocity collected by Bufton [19] [27, p. 87], and is presented in [16]:

$$u_L(z) = v_G + 30\, \mathrm{e}^{-\left(\frac{z-9400}{4800}\right)^2}.$$

It includes a constant mean value for the wind profile associated to the ground wind speed v_G (usually set to 8 m/s [16], or 5 m/s [14]), on which a Gaussian is added to represent the jet stream (at the altitude of the tropopause, here 9400 m). Initially, the model was given with a dependency to the elevation angle, as already presented in Section II-D for the Greenwood C_n^2 model.

The Bufton model is derived from rawinsonde measurements in Hawaii, and assumes z to be the altitude above the ground (located at 3048 m above the mean sea level). Hence, [28] recommends adding the ground altitude to the tropopause term (9400 m) when applying the model to other locations, even though it does not seem to be suited to other locations than Hawaii. The generalization of this model is given by [28]

$$u_L(z) = v_G + v_T\, \mathrm{e}^{-\left(\frac{z-h_T}{L_T}\right)^2}, \tag{7}$$

where v_G is the ground (or low altitude) wind speed, v_T is the tropopause wind speed, h_T is the tropopause altitude, and L_T is the thickness of the tropopause layer. For ground-to-satellite communications with moving satellites, an extra term is added to the model to take into account this motion as an apparent wind [4, p. 481], [29, p. 73]

$$u_L(z) = \omega_s z + v_G + v_T\, \mathrm{e}^{-\left(\frac{z-h_T}{L_T}\right)^2},$$

with ω_s the satellite slew rate [rad/s].

d: MODIFIED HUFNAGEL-VALLEY MODEL FOR OPTICAL COMMUNICATIONS

In order to obtain more realistic simulations of optical communication scenarios, at the European Space Agency (ESA) OGS site at Tenerife for example, the modified HV model has been suggested in [30] and [31]

$$C_n^2(z) = A\, \mathrm{e}^{-\frac{h_{\mathrm{GS}}}{700}}\, \mathrm{e}^{-\frac{z-h_{\mathrm{GS}}}{100}} + 2.7\times 10^{-16}\mathrm{e}^{-\frac{z}{1500}} + 0.00594\left(\frac{w}{27}\right)^2\left(\frac{z}{10^5}\right)^{10}\mathrm{e}^{-\frac{z}{1000}}.$$

Its main feature is the presence of h_{GS}, that corresponds to the ground station altitude (above mean sea level). Hence, the model is only suited for *altitudes z (above mean sea level)* greater than the ground station altitude.

e: PARAMETRIZATION FROM OT INTEGRATED PARAMETER MEASUREMENTS

If OT integrated parameters are measured at a location, a probable C_n^2 profile can be obtained from the HV model by fitting its parameters A and w. This approach requires knowledge of at least two integrated parameters, such as the coherence length r_0 and the isoplanatic angle θ_0, as presented in [32].

3) GENERALIZED HUFNAGEL-VALLEY MODEL

A generalization of the HV model is presented in [27, p. 85], that is convenient to particularize the HV model to different locations, as well as to add localized turbulent layers. The generalized HV form is

$$C_n^2(z) = A\, \mathrm{e}^{-\frac{z}{h_A}} + B\, \mathrm{e}^{-\frac{z}{h_B}} + C\, z^{10}\, \mathrm{e}^{-\frac{z}{h_C}} + D\, \mathrm{e}^{-\frac{(z-h_D)^2}{2d^2}}. \tag{8}$$

In (8), A is the ground turbulence strength and h_A is the altitude associated to its 1/e decay, while B and h_B have similar interpretations for the troposphere. The tropopause is modeled with C and h_C, and the last term actually enables to add localized turbulent layers, modeled by a Gaussian located at an altitude h_D, having a standard deviation (i.e., thickness) d and a C_n^2 magnitude of D. This last term can be repeated several times with different coefficients to model multiple isolated layers.

The benefit of this generalized model is that it can be easily adapted to any location where C_n^2 measurements are available, while being easily integrated to give OT integrated parameters (e.g., coherence length, isoplanatic angle). As an example, the values of the different coefficients involved for applying (8) to Mauna Kea, Hawaii, are given in [27, p. 86].

4) HUFNAGEL/ANDREWS/PHILLIPS MODEL AND EXTENSIONS

The Hufnagel/Andrews/Phillips (HAP) model aims at improving the modeling of the ground layer given by the HV model. Indeed, numerous measurements in the atmospheric BL showed a decrease of the C_n^2 profile following a $z^{-4/3}$ trend instead of the exponential decrease from the HV model (see Section IV-B). Hence, the BL term in (4) should be substituted with a term proportional to $z^{-4/3}$, as suggested in the HAP model [24]

$$C_n^2(z) = C_n^2(h_0)\left(\frac{h_0}{z}\right)^{4/3} + 2.7\times 10^{-16}\mathrm{e}^{-\frac{z}{1500}} + 0.00594\left(\frac{w}{27}\right)^2\left(\frac{z}{10^5}\right)^{10}\mathrm{e}^{-\frac{z}{1000}}, \tag{9}$$

for *altitudes z (in meters, above the mean sea level)* higher than the ground altitude, given by h_0. Expressing z as the altitude above the ground requires substituting $\left(\frac{h_0}{z}\right)^{4/3}$ by $\left(\frac{h_0}{z+h_0}\right)^{4/3}$ in (9). $C_n^2(h_0)$ is the ground C_n^2 value, hence corresponding to the A parameter in the HV model in (4). Due to this $z^{-4/3}$ trend, C_n^2 in the BL decreases faster with

increasing altitudes in the HAP model than in the HV model. However, for altitudes higher than 1 km, both models are similar.

Later revisions of the HAP model suggest the addition of a multiplicative factor $\tilde{M}$ for the FA part (troposphere + stratosphere), as well as a parametric exponent α instead of the fixed 4/3 exponent in the BL [33], leading to

$$C_n^2(z) = C_n^2(h_0)\left(\frac{h_0}{z}\right)^{\alpha} + \tilde{M}\Big[2.7\times10^{-16}\mathrm{e}^{-\frac{z+h_s}{1500}} + 0.00594\left(\frac{w}{27}\right)^2\left(\frac{z+h_s}{10^5}\right)^{10}\mathrm{e}^{-\frac{z+h_s}{1000}}\Big], \quad (10)$$

where h_s is the altitude of the ground above the mean sea level, and h_0 is the height above ground of the ground station or telescope. By explicitly taking h_s into account in (10), it is expressed with the altitude above the ground surface and not above sea level. Besides these two altitude parameters (h_s and h_0), the revision of the HAP model includes four other parameters: $\tilde{M}$ and α that are new additions to the model, and $C_n^2(h_0)$ and w, similar to previous HAP and HV models.

The parameter $\tilde{M}$ comes from an average value of the random background turbulence above 1 km and is typically close to unity [34, p. 88]. In [11], a seasonal variation of $\tilde{M}$ is presented based on one-year analysis of radiosonde observations near Munich, Germany. Modifying $\tilde{M}$ can also be useful to model percentiles of the turbulence statistics, i.e., modulate the amplitude of the HAP profile (or of the HV profile, if $\tilde{M}$ is added in (4) for example) in order to fit observed distributions of the C_n^2 profile above a given location. This is the approach followed in [35] with the HV model, using turbulence statistics collected in Korea, in 1999. A factor $\tilde{M} = 1$ is found for the median profile.

Regarding the exponent α, it varies between 4/3 during daytime and 2/3 at night. The following model has been suggested for daytime (between sunrise and sunset) [33]

$$\alpha = \begin{cases} -0.11(12-\mathrm{TH})^2 + 1.83(12-\mathrm{TH}) - 6.22 \\ 1.45 - 0.02(\mathrm{TH}-6)^2 \\ -0.048\,\mathrm{TH}^2 + 0.68\,\mathrm{TH} - 1.06, \end{cases}$$

where the first expression is valid for $0.75 < \mathrm{TH} < 3.5$, the second for $3.5 < \mathrm{TH} < 8.5$, and the last for $8.5 < \mathrm{TH} < 11.25$. It requires the knowledge of the sunrise and sunset times, as well as the computation of the temporal hour TH. The latter is given by equally dividing the time between sunrise (at t_{sunrise}) and sunset (at t_{sunset}) in 12 hours, and computing [36]

$$\mathrm{TH}(t) = \frac{t - t_{\text{sunrise}}}{\frac{t_{\text{sunset}} - t_{\text{sunrise}}}{12}}, \quad (11)$$

with t the local time. For nighttime (between sunset and sunrise), α is set to 2/3. This model for α has been obtained in Hollister, CA, and may require to be adapted to other locations [33].

For the parameter $C_n^2(h_0)$, corresponding to the C_n^2 value at the altitude h_0, i.e., at or near the ground, it is usually measured or estimated using ground layer C_n^2 models (see Section IV).

Finally, the wind speed parameter w is the same as for the HV model and can be computed using (3) with measured or modeled wind profiles. Recent works also explored its substitution by the wind speed profile $u_L(z)$ [37], [38].

B. TATARSKII-BASED MODELS

In his pioneering work, Tatarskii proposed the following equation to relate the temperature structure parameter C_T^2 to macroscale atmospheric quantities [2, p. 74]

$$C_T^2 = a^2\tilde{\alpha}L_0^{4/3}\left(\frac{\mathrm{d}T}{\mathrm{d}z}\right)^2, \quad (12)$$

where a^2 is an empirical constant, $\tilde{\alpha} = K_H/K_M$ is the ratio between the exchange coefficient for heat and momentum [39], L_0 is the outer scale of turbulence, and T is the mean temperature profile.

For the refractive index structure parameter C_n^2, (12) is

$$C_n^2 = a^2\tilde{\alpha}'L_0^{4/3}M^2,$$

with $M^2 = \left(\frac{\mathrm{d}n}{\mathrm{d}z}\right)^2$ and $\tilde{\alpha}'$ similar to $\tilde{\alpha}$. The latter is close to one [40] and usually neglected in the literature, such that the Tatarskii equation for C_n^2 is

$$C_n^2 = a^2L_0^{4/3}M^2, \quad (13)$$

with a value of 2.8 often used for a^2 [9, p. 173].

In (13), M is the vertical gradient of the mean (non-fluctuating) refractive index [9, p. 173], which can be computed directly from the derivative chain rule and refractive index expressions involving meteorological quantities, such as [4] and [41]

$$n = 1 + 10^{-6}\frac{77.6\,p}{T}\left(1 + \frac{7.52\times10^{-3}}{\lambda^2}\right), \quad (14)$$

with p the pressure expressed in hectopascal [hPa], T the temperature in kelvin [K], and λ the wavelength in micrometer [μm]. Equation (14) is valid for wavelengths between 0.36 and 3 μm according to [42], following the work of [43] and [44]. It is often approximated by its value for $\lambda = 0.5$ μm, leading to

$$n = 1 + 10^{-6}\frac{80\,p}{T}.$$

Using this approximate optical refractive index definition, M is given by

$$M = \frac{\mathrm{d}n}{\mathrm{d}z} = \frac{\partial n}{\partial T}\frac{\mathrm{d}T}{\mathrm{d}z} = -\frac{80\times10^{-6}p}{T^2}\frac{\mathrm{d}T}{\mathrm{d}z},$$

such that [4, p. 65], [3, p. 287]

$$C_n^2 = \left(\frac{80\times10^{-6}p}{T^2}\right)^2 C_T^2. \quad (15)$$

Other expressions for M can be found in the literature depending on the conservative variables used, as discussed

in [39]. Using the pseudopotential temperature $\tilde{\theta}$ defined by [2, p. 74], [9, p. 170]

$$\tilde{\theta} = T + \gamma z,$$

where $\gamma = \frac{g}{c_p}$ is the adiabatic lapse rate of dry air (equal to 9.8K/km in the troposphere), M is given by [2] and [39]

$$M = -\frac{80 \times 10^{-6} p}{T^2}\left(\frac{\mathrm{d}T}{\mathrm{d}z} + \gamma\right). \tag{16}$$

The use of the potential temperature θ leads to [39]

$$M = -\frac{80 \times 10^{-6} p}{T\theta}\frac{\mathrm{d}\theta}{\mathrm{d}z}.$$

For radiofrequencies, the contributions of the humidity in the refractive index should also be included in M, for which the developments can be found in [2, p. 75], [39], based on the refractive index expression in [41], [45], [46], [47], and [48], that is,

$$n = 1 + 10^{-6}\frac{77.6}{T}\left(p + \frac{4810\, e}{T}\right), \tag{17}$$

where e is the partial pressure of water vapor in hectopascal [hPa], related to the specific humidity q by $e \approx 1.62\, pq$ [39], the accurate expression being given in [49, p. 41]. Equation (17) is valid for frequencies ranging from 1 MHz to 30 GHz [41] and in the temperature range from −50 to 40°C.

In addition to defining M, applying the Tatarskii equation (13) necessitates a parametrization of the outer scale L_0. This section reviews the various models for L_0 that have been proposed in the literature.

1) DEWAN MODEL AND EXTENSIONS (OUTER SCALE MODELS USING WIND SHEAR AND TEMPERATURE GRADIENT)

Among the Tatarskii-based models, the Dewan model, and its extensions, are very often used in the literature thanks to their simplicity of application. Indeed, they can easily be applied to meteorological quantities coming from radiosonde observations [50], [51], or from numerical weather predictions (NWP) [52], [53], [54], [55]. All are based on the form of the Tatarskii equation in (13) [56, p. 2], where the outer scale L_0 comes from different parametrizations. Those parametrizations are derived from empirical observations and fitting, involving the horizontal wind shear S and the vertical gradient of temperature $\frac{\mathrm{d}T}{\mathrm{d}z}$, that is,

$$L_0^{4/3} = f\left(S, \frac{\mathrm{d}T}{\mathrm{d}z}\right).$$

The distinction between the Dewan model and its different extensions is in the expression of the function $f\left(S, \frac{\mathrm{d}T}{\mathrm{d}z}\right)$, as presented in the paragraphs below.

As detailed in [56, p. 1], Dewan models are only suited for modeling the troposphere and stratosphere, and not the BL.

a: DEWAN MODEL

The Dewan model, initially referred to as the AFGL model, has been presented in 1993 in [56]. It relies on (13), using the expression for M in (16) with a coefficient 79 instead of 80. In order to model the outer scale of turbulence L_0, a rule of thumb, inspired by the literature at that time, is used: L_0 is assumed to be of the order of 0.1 times the thickness of the turbulent layer [56, p. 2]. As a result, knowledge of the turbulent layer thickness enables to determine L_0.

Relying on high resolution (vertical resolution of 10 meters) stratospheric velocity profiles obtained by rocket laid smoke trails, the turbulent layer thickness is estimated from the Richardson number Ri given by

$$\mathrm{Ri} = \frac{N^2}{S^2},$$

where $N^2 = \frac{g\left(\frac{\mathrm{d}T}{\mathrm{d}z} + \gamma\right)}{T}$ is the "buoyancy frequency" (Brunt-Väisälä frequency), and $S = \sqrt{\left(\frac{\mathrm{d}u}{\mathrm{d}z}\right)^2 + \left(\frac{\mathrm{d}v}{\mathrm{d}z}\right)^2}$ is the wind shear (u and v are the horizontal wind components). A layer is considered turbulent if the Richardson number is smaller than a threshold, usually set to 0.25 [57, p. 175]. In [56], a value of 0.5 is chosen, and the turbulent layers can be identified from the velocity measurements and the criterion $S^2 > 2N^2$. Then, their thickness is computed. This approach is further detailed in [56], and has been extended in [58].

Finally, the thickness of the different turbulent layers is associated to the large scale shears measured by radiosonde observations (vertical resolution of 300 meters). A statistical relationship is determined by averaging the layer thicknesses over 300-meter slabs, leading to the following fit:

$$Y = \begin{cases} 1.64 + 42.0\, S_{\mathrm{raw}} & \text{(troposphere)} \\ 0.506 + 50.0\, S_{\mathrm{raw}} & \text{(stratosphere)}, \end{cases} \tag{18}$$

where Y corresponds to the logarithm in base 10 of the average turbulent layer thicknesses. S_{raw} is the wind shear S as measured by the radiosondes (rawinsondes), having a 300-meter vertical resolution. Hence, the outer scale is modeled by

$$L_0^{4/3} = 0.1^{4/3}\, 10^{Y}. \tag{19}$$

Equations (18) and (19) are simple to use, but it is important to consider the conditions under which they have been obtained, highlighting their limitations:

- First, the fitting coefficients were obtained by using radiosonde observations with a 300-meter vertical resolution. As a result, this same resolution should be used when computing the wind shear to insert in (18) [56, p. 3, 28].
- Second, (18) requires the knowledge of the tropopause altitude, separating the troposphere and the stratosphere. Moreover, only stratospheric velocity profiles have been measured, hence the tropospheric part of the model may not be very accurate [56, p. 7].
- Finally, some upper limits on the computed meteorological quantities from the radiosonde observations are used:

wind shear larger than 0.04 s^{-1} are set to 0.04 s^{-1} in the model, and tropospheric temperature gradients are set to 10^{-3} K/m whenever they exceed zero [56, p. 8].

Those limitations are rarely taken into account while applying the Dewan model to new observations at other locations.

Validation of the Dewan model is presented in the original paper [56], comparing the model predictions with thermosonde measurements from the CLEAR-1 and CLEAR-3 programs in New Mexico (USA), and from the Hawaiian program in 1984. Other values for the coefficients in (18) fitted specifically for the Terskol Observatory (Caucasus, Russia) can be found in [59].

b: JACKSON MODEL

In 2004, a report from the Air Force Research Laboratory (AFRL), written by Jackson, presented some modified Dewan parametrizations for the outer scale. The approach used to obtain the new parametrizations is different from the one previously followed by Dewan, and relies on statistical regressions. Indeed, from C_n^2 measurements obtained by thermosondes, one can invert the Dewan model and isolate the Y parameter, called Y_{obs} in [60, p. 4], that is,

$$Y_{\text{obs}} = \log_{10}\left(\frac{C^2_{n,\text{meas}}}{2.8\, M^2 0.1^{4/3}}\right).$$

From scatter plots of Y_{obs} against wind shear, measured during the Holloman Spring 1999 campaign, little relationship was found between these two parameters. However, scatter plots involving the vertical gradient of temperature showed stronger relationships, motivating its use for predicting L_0. Consequently, several regressions involving linear functions of the wind shear and up to fourth-order polynomials of the temperature vertical gradient have been derived and presented in [60]. Special care has been devoted to the lower troposphere (from 1572 to 5472 meters at Holloman, New Mexico), establishing valid parametrizations for this part of the atmosphere. All parametrizations can be found in [60, p. 13, 16, 19]. Only the most complex parametrizations are presented below, using the fourth-order polynomials of the temperature vertical gradient:

$$Y=\begin{cases} 2.9767 + 27.9804\, S + 2.9012\, \frac{\mathrm{d}T}{\mathrm{d}z} + 1.1843 \left(\frac{\mathrm{d}T}{\mathrm{d}z}\right)^2 \\ \quad +0.1741 \left(\frac{\mathrm{d}T}{\mathrm{d}z}\right)^3 + 0.0086 \left(\frac{\mathrm{d}T}{\mathrm{d}z}\right)^4 \\ 0.7152 + 30.6024\, S + 0.0003\, \frac{\mathrm{d}T}{\mathrm{d}z} - 0.0057 \left(\frac{\mathrm{d}T}{\mathrm{d}z}\right)^2 \\ \quad -0.0016 \left(\frac{\mathrm{d}T}{\mathrm{d}z}\right)^3 + 0.0001 \left(\frac{\mathrm{d}T}{\mathrm{d}z}\right)^4 \\ 0.6763 + 8.1569\, S - 0.0536\, \frac{\mathrm{d}T}{\mathrm{d}z} + 0.0084 \left(\frac{\mathrm{d}T}{\mathrm{d}z}\right)^2 \\ \quad -0.0007 \left(\frac{\mathrm{d}T}{\mathrm{d}z}\right)^3 + 0.0002 \left(\frac{\mathrm{d}T}{\mathrm{d}z}\right)^4 \end{cases}, \tag{20}$$

with the first equality valid in the lower troposphere, the second in the troposphere, and the last in the stratosphere. The expressions in (20), transcribed from Jackson's report, use the temperature vertical gradient expressed in [°C/km]. A reasonable fit for both the troposphere and the stratosphere is also presented in [60, p 21]. All fits were obtained from the thermosonde observations of the AFRL Holloman Spring 1999 campaign. As in the original model from Dewan, a vertical resolution of 300 meters is chosen.

The modified Dewan models have been applied to eight thermosonde launches conducted during the Holloman Spring 1998 campaign (launches HMNSP104, HMNSP107, HMNSP108, and HMNSP111 to HMNSP115). Most improvements compared to the Dewan model have been found to be located in the lower troposphere part. Nevertheless, the model has been developed and tested for only one location (Holloman, New Mexico), and for one season (spring), hence its performance for other locations and seasons are uncertain [60, p. 61].

c: HMNSP99 MODEL

The HMNSP99 model, attributed to [61], is another parametrization of L_0 inspired by the Dewan model. It relies on (19) and makes use of linear relationships of the wind shear and the temperature vertical gradient, that is, [51], [53]

$$Y = \begin{cases} 0.362 + 16.728\, S - 192.347\, \frac{\mathrm{d}T}{\mathrm{d}z} & \text{(troposphere)} \\ 0.757 + 13.819\, S - 57.784\, \frac{\mathrm{d}T}{\mathrm{d}z} & \text{(stratosphere),} \end{cases}$$

with $\frac{\mathrm{d}T}{\mathrm{d}z}$ in [K/m]. This model is applied in numerous recent papers [50], [51], [53]. The influence of the vertical resolution of radiosonde observations used with the HMNSP99 model is briefly studied in [62].

d: WSTG MODEL

Based on radiosonde and thermosonde observations collected from November to December 2017 in Sanya (Hainan island, China), the Wind Shear and Temperature Gradient (WSTG) model has been developed [50]. As the HMNSP99 model, it depends linearly on the wind shear and the vertical temperature gradient. However, the model originality lies on the boundary between the different parametrizations that depends on the values of S and $\frac{\mathrm{d}T}{\mathrm{d}z}$, and not on the altitude. Indeed, the outer scale is modeled by (19), with

$$Y = \begin{cases} 0.835 - 37.164\, S - 306.034 \frac{\mathrm{d}T}{\mathrm{d}z}, & S < 0.016 \cap \frac{\mathrm{d}T}{\mathrm{d}z} < 0 \\ 0.825 + 66.9\, S - 52.783 \frac{\mathrm{d}T}{\mathrm{d}z}, & S < 0.016 \cap \frac{\mathrm{d}T}{\mathrm{d}z} > 0 \\ 0.715 + 52.907\, S - 102.515 \frac{\mathrm{d}T}{\mathrm{d}z}, & S > 0.016 \cap \frac{\mathrm{d}T}{\mathrm{d}z} < 0 \\ 2.215 - 9.882\, S - 101.666 \frac{\mathrm{d}T}{\mathrm{d}z}, & S > 0.016 \cap \frac{\mathrm{d}T}{\mathrm{d}z} > 0 \end{cases}$$

The symbol $\cap$ denotes the intersection, meaning that both conditions should be fulfilled. This model derives from

observed increases in the correlations of statistical operators when wind shears are larger than 0.016 m/s, and coefficients have been obtained by minimizing the residual sum of squares between measured values and estimations. A vertical resolution of 100 meters is used.

2) ALTITUDE-DEPENDENT OUTER SCALE MODELS

As an alternative to more complex models of the outer scale depending on meteorological parameters, simple altitude-dependent models have been suggested in the literature. All of them are derived from C_n^2 (or C_T^2) measurements (meas.), fitting for the values of L_0 giving C_n^2 profiles as close as possible to the measurements when using the Tatarskii model in (13). Alternatively, the observed outer scale profile can be computed by isolating L_0 in the Tatarskii model, i.e.,

$$L_{0,\text{meas}} = \left(\frac{C_{n,\text{meas}}^2}{a^2 \, M^2} \right)^{3/4}. \tag{21}$$

The vertical resolution chosen to compute the outer scale from the measurements is important. Indeed, coarse vertical resolution can lead to average L_0 values over large atmospheric slabs, that may not be representative of the physical outer scale (underestimation). A possible scaling argument is presented in [63], relying on an estimation of the fractional turbulent volume inside the atmospheric slabs. For example, if 5% of the volume is considered turbulent, the obtained L_0 values should be scaled by 20 [8]. Despite this simple approximation, the effect of various vertical resolutions for the determination of L_0 requires further research, and it is recommended to use the same resolution as was used in the design of the different models when applying them.

a: COULMAN MODEL AND EXTENSIONS

The Coulman model has been obtained from SCIntillation Detection And Ranging (SCIDAR) observations at the Observatoire de Haute-Provence (France), and at the McDonald Observatory (Texas, USA) in 1985 [64]. SCIDAR observations provided measurements of C_n^2 profiles with a resolution of ∼800 m, while nearby radiosonde launches enabled to compute M^2 with a vertical spacing on the order of 1000 m. By segregating the data over 1-km slabs from 2 km to 17 km of altitude, the following fit has been computed in order to model the observed altitude dependency in L_0:

$$L_0(z) = \frac{4}{1 + \left(\frac{z-8500}{2500} \right)^2}, \tag{22}$$

with z the altitude in meters ($2000 < z < 17000$).

Later application of this model to SCIDAR observations at the European Southern Observatory, La Silla (Chile), in 1986, showed a similar altitude dependency [64]. Fitting these new observations gave

$$L_0(z) = \frac{5}{1 + \left(\frac{z-7500}{2000} \right)^2}, \tag{23}$$

that is similar to (22). Both (22) and (23) retrieves outer scale no larger than 5 meters.

In [65], an updated Coulman profile is presented for the Paranal observatory (Chile), following the Paranal Seeing Campaign in March 1992. For an altitude greater than the mountain summit ($z > z_0 = 2636$ meters), L_0 is modeled by

$$L_0 = \frac{2}{3} \left(\frac{4}{1 + \left(\frac{z-8500}{2500} \right)^2} + 8 \, \mathrm{e}^{\frac{z_0 - z}{1500}} \right).$$

This fit follows observations of large outer scale values at the ground level.

Furthermore, a revised version of the Coulman model for the Observatorio del Teide (Tenerife, Spain) is also presented in [66], following SCIDAR observations with a 300-meter resolution:

$$L_0(z) = \frac{5.2}{1 + \left(\frac{z-7526}{2404} \right)^2}.$$

b: BELAND & BROWN MODEL

The Beland & Brown model is a deterministic C_n^2 model making use of the Tatarskii equation with the following parametrization for L_0 [63]

$$L_0(z) = 0.307 - 0.0324\,(z-17) + 0.00167\,(z-17)^2 + 0.000476\,(z-17)^3,$$

with z *the altitude above sea level in kilometres*, ranging from 17 to 30 km. It has been derived from thermosonde and radiosonde measurements during nighttime in New Mexico (8 flights) and Hawaii (7 flights), having a vertical resolution of 20 meters. It only describes the lower stratosphere, and has been obtained using a 500-meter window average for computing the outer scale L_0, and by fitting a cubic polynomial to all the data. It gives values of L_0 between 0.25 m and 1 m.

c: BOUNDARY LAYER OUTER SCALE MODELS

Some simple outer scale models in the BL can be found in the literature. This is the case of the Tatarskii expression [8, p. 177]

$$L_0(z) = \begin{cases} 0.4 & \text{for } z < 1 \\ 0.4\,z & \text{for } 1 < z \leq 25, \end{cases}$$

with z in meters (altitude above the ground). The completion of the Tatarskii outer scale expression with the Fried model [67], given by

$$L_0(z) = 2\sqrt{z},$$

for z ranging from the surface to 10 km, can be found in [65].

Alternatively, a fitted L_0 profile in the BL from 0 to 1 km above the ground has been presented in [68]. It relies on radiosonde and thermosonde measurements at several

astronomical sites, recording an average L_0 profile (with a 25-meter vertical resolution) given by

$$L_0(z) = 3.21\, z^{-0.11},$$

where z is the altitude above the ground expressed in meters and lower than 1000 m.

3) VANZANDT MODEL (PROBABILISTIC APPROACH)

The VanZandt model, from the National Oceanic and Atmospheric Administration (NOAA) is a probabilistic model based on the Tatarskii equation. It has been derived from Very High Frequency (VHF) Doppler radar measurements, and provides an estimation of C_n^2 from radiosonde observations with a vertical resolution of 150 m (at best) [40], [69]. This model is suited both for radiofrequency C_n^2 [70], [71] and optical C_n^2 [9, p. 223], [8, p. 176], [64]. The main reference presenting the model and its necessary hypotheses is the NOAA Technical Report from Warnock and VanZandt, published in 1985 [72].

VanZandt model makes use of (13) with a^2 approximated by 2.8 and M given by [72, p. 9]

$$M = -77.6 \times 10^{-6} \frac{p}{T} \frac{N^2}{g} \left[1 + 15500 \frac{q}{T} - \frac{15500}{2} \frac{q' g}{N^2 T} \right],$$

where $N^2 = g \frac{\mathrm{d}(\ln \theta)}{\mathrm{d}z}$, $q' = \frac{\mathrm{d}q}{\mathrm{d}z}$ with q the specific humidity, and p is in [hPa]. Since the radiosonde observations used in [72] have a resolution of 150 meters (or coarser), the atmosphere is considered to be split in slabs of 150 meter thickness (or greater). Hence, C_n^2 cannot be computed for each fine-scale turbulent layer (i.e., layers being 10-meter thick or thinner), and only an estimation of the mean C_n^2 over the slab is available, denoted $\bar{C}_n^2$. This lack of data availability led Warnock and VanZandt to use a probabilistic approach, expressing the $\bar{C}_n^2$ estimate as [72, p. 9]

$$\bar{C}_n^2 = \int_{L_{\min}}^{L_{\max}} \mathrm{d}L \iint_{\mathrm{Ri}<\mathrm{Ri}_c} \mathrm{d}S\, \mathrm{d}N^2 \int_{-\infty}^{\infty} \mathrm{d}q'\, p_{L,S,N^2,q'}\, C_n^2, \tag{24}$$

where the dependency of $p_{L,S,N^2,q'}$ and C_n^2 in (L, S, N^2, q') is implicit. Equation (24) involves the Richardson number $\mathrm{Ri} = N^2/S^2$, the critical value of the Richardson number Ri_c chosen to be 0.25, and the multivariate Probability Density Function (PDF) $p_{L,S,N^2,q'}$ of the outer scale L, the wind shear S, N^2, and q'.

Assuming that q' and N^2 are fully (anti)correlated, and that the PDFs of the outer scale, the wind shear, and N^2 are independent, the estimate $\bar{C}_n^2$ can be computed from [72, p. 13]

$$\bar{C}_n^2 = 2.8\, M_0^2\, \tilde{R} \int_{L_{\min}}^{L_{\max}} L^{4/3}\, p_L\, \mathrm{d}L \times \int_0^{\infty} p_S\, \mathrm{d}S \int_{-\infty}^{S^2 \mathrm{Ri}_c} (N^2)^2\, p_{N^2}\, \mathrm{d}N^2.$$

The factor M_0 is equal to $M_0 = -77.6 \times 10^{-6} \frac{p}{T} \frac{1}{g}$, while $\tilde{R}$ is

$$\tilde{R} = \left[1 + 15500 \frac{q}{T} - \frac{15500}{2} \frac{q' g}{N^2 T} \right]^2.$$

For optical C_n^2 estimates, the humidity variations are neglected and $\tilde{R}$ reduces to 1 [72, p. 14]. The probability distributions are assumed to be the following: uniform distribution for L, Gaussian distribution for N^2, and Gaussian distributions for each component of the velocity vector, giving a Rice distribution for S [72, p. 13]. The distribution parameters are estimated from the radiosonde measurements over the atmospheric slabs. A detailed numerical implementation of the model can be found in [72].

4) ALTERNATIVE LENGTH SCALES

The outer scale L_0, defined as the upper limit of the inertial range, can be related to various length scales available in the literature. As detailed in [73], commonly used outer scales are the Ozmidov length scale L_{OZ} and the Corrsin length scale L_C, given by [74], [75]

$$L_{\mathrm{OZ}} = \sqrt{\frac{\varepsilon}{N^3}} \qquad \text{and} \qquad L_C = \sqrt{\frac{\varepsilon}{S^3}},$$

where ε is the mean dissipation rate of turbulent energy. From these definitions, turbulent eddies smaller than the Ozmidov length scale L_{OZ} are not influenced by the buoyancy, while eddies smaller than the Corrsin length scale L_C are not impacted by the shear. As a result, eddies smaller than L_{OZ} and L_C are considered isotropic [73]. The ratio L_C/L_{OZ} is directly related to the Richardson number since $L_C/L_{\mathrm{OZ}} = (N/S)^{3/2} = \mathrm{Ri}^{3/4}$.

Practical computations of L_{OZ} or L_C, for example from radiosonde observations, are made difficult by the presence of ε in their definitions. Nevertheless, substitutes for these quantities, and hence for the outer scale L_0, have been suggested in the literature. When used for L_0 in (13), they enable to model C_n^2.

a: THORPE SCALE

The Thorpe scale L_T is often used as a substitute for the Ozmidov scale L_{OZ} in stably stratified fluids (see [76], [77] and references therein for the existing proportionality relationships between L_T and L_{OZ}). Initially, it has been presented by Thorpe in 1977 to analyse the turbulence in oceans and lakes from water density and potential temperature profiles [78]. Since then, it has been demonstrated to also apply to the atmosphere [77].

The approach is empirical and estimates the scales of overturns in the measured profiles, caused by the turbulence. Indeed, it relies on the assumption that, under stable conditions, density or potential temperature profiles should be monotonic. Hence, inversions in these profiles come from turbulent mixing [79].

In order to estimate L_T, observed profiles are rearranged into monotonic profiles containing no inversion, i.e., sorting

the different measured samples at each sampled altitude (or depth, in water). The required displacement to create the stable profiles is recorded at each altitude (respectively, each depth), the Thorpe scale L_T being simply the RMS of this displacement [77]. Instead of the RMS of the displacement, some authors use its absolute value [62], [66], [80].

From the measured Thorpe scale L_T, the temperature structure parameter C_T^2 can be estimated using [76], [81]

$$C_T^2 = c_T \, L_T^{4/3} \left(\frac{\mathrm{d}\theta_s}{\mathrm{d}z} \right)^2, \tag{25}$$

with θ_s the sorted potential temperature profile (used as an estimation of the average profile), and c_T a proportionality constant depending on a^2 in (13) and the relationship between L_{OZ} and L_T. From the C_T^2 profile, the C_n^2 profile is obtained using (15).

The literature behind the Thorpe length scale is rich, with applications both in oceanography and atmospheric sciences [79], [81], [82], [83]. The influence of instrumental noise in the estimation of L_T is rather important, and must be handled appropriately [84].

b: ELLISON SCALE

Similarly to the Thorpe scale, the Ellison scale L_E is sometimes used to model C_n^2, with a similar equation as (25) where L_T is substituted by L_E [73]. The Ellison scale has been originally suggested by Ellison in 1957 and corresponds to the ratio between the standard deviation of the density fluctuations and the vertical gradient of the density [85]. In terms of potential temperature, it is expressed by [73]

$$L_E = \frac{\sigma_\theta}{\left(\frac{\mathrm{d}\bar{\theta}}{\mathrm{d}z} \right)},$$

with σ_θ^2 the variance of the potential temperature fluctuations.

Applications of the Ellison scale to radiosonde observations can be found in [51] and [80]. In [51], the Ellison scale is estimated by

$$L_E = \left| \frac{\Delta\theta}{\left(\frac{\mathrm{d}\theta_s}{\mathrm{d}z} \right)} \right|,$$

where $\Delta\theta(z) = \theta(z) - \theta_s(z)$, i.e., the difference between the measured potential temperature and its sorted profile.

c: DEARDOFF LENGTH SCALE

In [86], the Deardoff length L_D is used in Tatarskii equation for stable layers. It is given by [87],

$$L_D = \sqrt{\frac{2k_\epsilon}{\frac{g}{\theta_v}\frac{\partial\theta_v}{\partial z}}}, \tag{26}$$

where the parameter ϕ_3 is equal to 0.78 [86]. Equation (26) involves the Turbulent Kinetic Energy (TKE) depicted by k_ϵ, the gravity of Earth g, and the virtual potential temperature θ_v taking into account humidity and given by $\theta_v = \theta(1+0.61 q_v)$ for unsaturated air with mixing ratio q_v [57, p. 7]. These different quantities can be obtained from NWP simulations in [86].

d: LOUIS AND TJERNSTRÖM MIXING LENGTH

In [88], the mixing length of sensible heat is related to the gradient Richardson number Ri, following the work of [89],

$$L_H = \tilde{l}_0 \left(1 + 15 \, \mathrm{Ri} \sqrt{1 + 5 \, \mathrm{Ri}} \right)^{-1/2}. \tag{27}$$

The variable $\tilde{l}_0$ represents an asymptotic mixing length, equal to 450 m in [89], and 23 m in [88].

Equation (27) is used in [90], [91] for the parametrization of L_0 in the Tatarskii equation.

e: TEMPERATURE-BASED MIXING SCALE

In [92], the outer scale L_0 is estimated from the mixing scale Δz_0 at which the equality between the temperature systematic difference and the temperature random difference is reached [93], i.e.,

$$[\langle T(z) \rangle - \langle T\,(z + \Delta z_0) \rangle]^2 = \left\langle [T(z) - T\,(z + \Delta z_0)]^2 \right\rangle.$$

The outer scale is then obtained from

$$L_0(z) \approx \left(2.8 \left(1 + \frac{\gamma}{\frac{\mathrm{d}T}{\mathrm{d}z}} \right)^2 \right)^{-3/4} \Delta z_0.$$

5) COMBINATION OF LENGTH SCALES

As shown above, many models for the outer scale L_0, or for alternative scales, are available. Some of them are empirically-based, others require some physical understanding of atmospheric turbulence. Recently, new models have been suggested by combining the previous models, either with new analytical expressions, or with weights computed numerically.

a: WSPT MODEL

The Wind Speed and Potential Temperature (WSPT) model is inspired by the Thorpe scale and the Dewan model, combining the meteorological quantities involved in each model. Indeed, the WSPT scale L_W is defined by [94]

$$L_W = \sqrt{\frac{\Delta\theta}{\frac{\mathrm{d}\theta_s}{\mathrm{d}z}} \left(\frac{u\,v}{S^2} \right)^{1/2}},$$

where all quantities have been defined previously. It comes from the product between a temperature scale given by $\frac{\Delta\theta}{\frac{\mathrm{d}\theta_s}{\mathrm{d}z}}$, and a wind speed scale obtained from $\left(\frac{u\,v}{S^2} \right)^{1/2}$. C_T^2 is then estimated using

$$C_T^2 = c_w \, L_W^{4/3} \left(\frac{\mathrm{d}\theta_s}{\mathrm{d}z} \right)^2, \tag{28}$$

with c_w a proportionality constant, calculated to ensure agreement between the measured C_T^2 and its estimation from (28).

The WSPT model has been validated with thermosonde measurements from Rongcheng and Maoming, in China. A vertical resolution of 100 m is used. A median c_w of 0.3 has been found for Rongcheng for example.

b: MULTI-MODEL ENSEMBLE PATTERN

The Multi-model Ensemble Pattern (MEP) approach presented in [80] aggregates different C_n^2 and outer scale models into a single C_n^2 estimation. The different models are: Hufnagel-Valley 5/7, Dewan, HMNSP99, Thorpe, Ellison, WSPT, and WSTG. For each model, a weighting coefficient (between 0 and 1, with their summation equal to 1) is computed empirically, based on the different model performance on predicting the measured C_n^2 profiles, ensuring that larger coefficients will be given to models offering more accurate predictions. Then, the MEP final prediction comes from the summation of each model prediction, weighted by the coefficients previously computed. Details about the combination approach can be found in [80], where the MEP approach has been applied to radiosonde and thermosonde soundings in China.

C. TRINQUET-VERNIN MODEL

The Trinquet-Vernin model [95], published in 2007, relies on the potential temperature vertical gradient and the wind-shear to predict the temperature structure parameter C_T^2 profile. A C_n^2 profile can then be computed, using (15).

Defining the vertical gradient of the potential temperature by $\chi = \frac{\mathrm{d}\theta}{\mathrm{d}z}$ and using the wind shear $S = \sqrt{\left(\frac{\mathrm{d}u}{\mathrm{d}z}\right)^2 + \left(\frac{\mathrm{d}v}{\mathrm{d}z}\right)^2}$, the core equation of the TV model is [95]

$$\frac{C_T^2(z)}{\langle C_T^2(z)\rangle_m} = \left(\frac{\chi(z)}{\langle\chi(z)\rangle_m}\right)^a \left(\frac{S(z)}{\langle S(z)\rangle_m}\right)^b, \tag{29}$$

where $\langle C_T^2(z)\rangle_m$ represents the median C_T^2 profile, $\langle\chi\rangle_m$ is the median potential temperature profile, and $\langle S\rangle_m$ is the median wind shear profile. The exponents a and b have been deduced from the analysis of balloon measurements of C_T^2 and meteorological parameters at diverse locations (mostly astronomical sites). Thanks to least-squares fits between the measured and modeled C_T^2 profiles, a value of 1 has been found for a, while b is set to $1/2$ (see [95] for the standard deviations of those parameters depending on the atmospheric layer and on the vertical resolution). The exponent $a = 1$ for the potential temperature gradient is in disagreement with Tatarskii equation (13), and potentially highlights the limitation of Tatarskii-based models to describe the turbulence at macroscopic scales [95].

For practical use, the TV model in (29) is usually rewritten with the function $\phi(z)$, defined as [96]

$$\phi(z) = \frac{\langle C_T^2(z)\rangle_m}{\langle\chi(z)\rangle_m \langle S(z)\rangle_m^{1/2}},$$

leading to

$$C_T^2(z) = \phi(z)\, \chi(z)\, S(z)^{1/2}. \tag{30}$$

The function $\phi(z)$ is deduced from the balloon measurements, with an example given in Table 2, specifying its values in the BL and in the FA [97]. However, recent works suggest that $\phi(z)$ is site-dependent and should be empirically "learned" at the site of interest, i.e., using balloon measurements at this site [96]. A diurnal variation of $\phi(z)$ has also been found in [96].

A major limitation of the TV model is related to the unitary exponent a of the potential temperature gradient in (30). Indeed, this prevents the model to be applied to convective cases, i.e., cases where the potential temperature gradient is negative [95]. Convective regimes, which occur mostly during daytime and close to the ground, are thus excluded. A possible solution to circumvent this limitation is to use an alternative C_n^2 model for the convective regions, such as a Tatarskii-based model, as presented in [96].

Recent applications of the TV model with NWP software can be found in [92], [96], and [98].

TABLE 2. Values of the function $\phi(z)$ deduced from balloon measurements (table reproduced from [97]).

Boundary layer		Free atmosphere	
Altitude z [m]	$\phi(z)$	Altitude z [km]	$\phi(z)$
5	2.8350	1.5	0.2202
55	0.7826	2.5	0.1233
105	0.2851	3.5	0.1221
155	0.2248	4.5	0.1117
205	0.2334	5.5	0.0796
255	0.2369	6.5	0.0766
305	0.1394	7.5	0.0947
355	0.1698	8.5	0.0824
405	0.1351	9.5	0.0856
455	0.1152	10.5	0.0796
505	0.1202	11.5	0.0596
555	0.1242	12.5	0.0445
605	0.1528	13.5	0.0453
655	0.1258	14.5	0.0386
705	0.1038	15.5	0.0492
755	0.0960	16.5	0.0455
805	0.0832	17.5	0.0459
855	0.1062	18.5	0.0397
905	0.0947	19.5	0.0413
955	0.1023		

IV. BOUNDARY AND SURFACE LAYER MODELS

Most of the non-parametric and parametric models presented in Sections II and III are valid for the FA, i.e., the part of the troposphere that is not influenced by the Earth's surface. Nevertheless, the atmospheric BL, defined in [57, p. 2] as "*the part of the troposphere that is directly influenced by the presence of the Earth's surface, and responds to surface forcing with a timescale of about an hour or less*", plays a major role in the modeling of optical turbulence.

Indeed, the atmospheric BL has important diurnal variations impacting atmospheric turbulence and the associated C_n^2 values. As shown from ground C_n^2 measurements in the Tularosa basin (desert), New Mexico (USA), given in [99] and reproduced in Figure 4, ground C_n^2 tends to peak

around noon, i.e., when solar heating of the ground is the largest. Minima occur near sunrise and sunset, associated to neutral events during which the soil and air temperature are similar. Nevertheless, such behaviour is site-dependent, as illustrated in various models and measurements from the literature [100], [101]

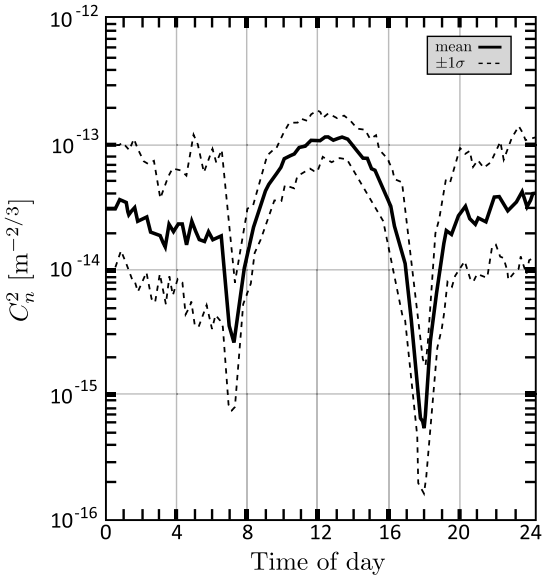

FIGURE 4. Illustration of diurnal variations of ground C_n^2 (reproduced from [99]).

The atmospheric BL over land and in high pressure regions has a well-defined structure showing a diurnal cycle, given in Figure 5. It is separated in [57, p. 10]:

- the *surface layer* (SL), that is, the layer the closest to the ground, where "turbulent fluxes and stress vary by less than 10% of their magnitude,"
- the *mixed layer*, occurring in daytime and mostly driven by convection, such as heat transfer from the warm ground surface,
- the *residual layer*, arising from the decay of the mixed layer in nighttime,
- the *stable (nocturnal) boundary layer*, that is, "the bottom portion of the residual layer, transformed by its contact with the ground into a stable BL".

The identification of the different parts of the BL can usually be achieved with the knowledge of virtual potential temperature profiles and is important as different C_n^2 models have been developed according to the layer type. Surface layer C_n^2 models are introduced in Section IV-A, while daytime and nighttime profiles over the whole BL are presented in Section IV-B.

A. SURFACE LAYER AND GROUND C_N^2

Modeling of SL C_n^2 can be achieved by regression models based on empirical observations (Section IV-A1), or from physical insights from the similarity theory (Section IV-A2).

1) REGRESSIONS OF MACROSCALE METEOROLOGICAL PARAMETERS

C_n^2 models based on regressions of macroscale meteorological parameters give access to the surface C_n^2 value from measurements of surface meteorological parameters, such as temperature, relative humidity, wind speed. They are designed based on simultaneous measurements of C_n^2 and meteorological parameters at a given location, using empirical fitting of the collected data.

a: SADOT-KOPEIKA MODELS

The Sadot-Kopeika models have been presented in 1992 and provide an estimation of the C_n^2 ground value based on regressions [36]. The models have been established from angle-of-arrival and amplitude fluctuation measurements over a laser horizontal path in the Israeli desert (Beer-Sheva). In total, over 70 experiments have been conducted during three months in 1990 (late winter, spring, and early summer), in day and night conditions, with recording of meteorological parameters. Based on the collected measurements, two polynomial regression models have been suggested, where their coefficients have been found by minimizing the least-square error.

The first model is based on the ground temperature T [K], relative humidity RH [%], and wind speed u_L [m/s]. It also involves the temporal hour weight W(TH) given in Table 3, making use of the temporal hour TH as defined in (11). It is given by

$$C_n^2 = a_1 W + b_1 T + c_1 \mathrm{RH} + c_2 \mathrm{RH}^2 + c_3 \mathrm{RH}^3 + d_1 u_L + d_2 u_L^2 + d_3 u_L^3 + e, \quad (31)$$

with the coefficients $a_1, b_1, \ldots, e$ given in Table 4. The model in (31) is suited for practical use, as it is simple and involves standard meteorological parameters.

TABLE 3. Temporal hour weights for Sadot-Kopeika models (table reproduced from [36]).

	Temporal hour (TH) interval	Relative weight (W)
	until -4	0.11
	-4 to -3	0.11
	-3 to -2	0.07
	-2 to -1	0.08
	-1 to 0	0.06
sunrise	0 to 1	0.05
	1 to 2	0.1
	2 to 3	0.51
	3 to 4	0.75
	4 to 5	0.95
	5 to 6	1.00
	6 to 7	0.90
	7 to 8	0.80
	8 to 9	0.59
	9 to 10	0.32
	10 to 11	0.22
sunset	11 to 12	0.10
	12 to 13	0.08
	over 13	0.13

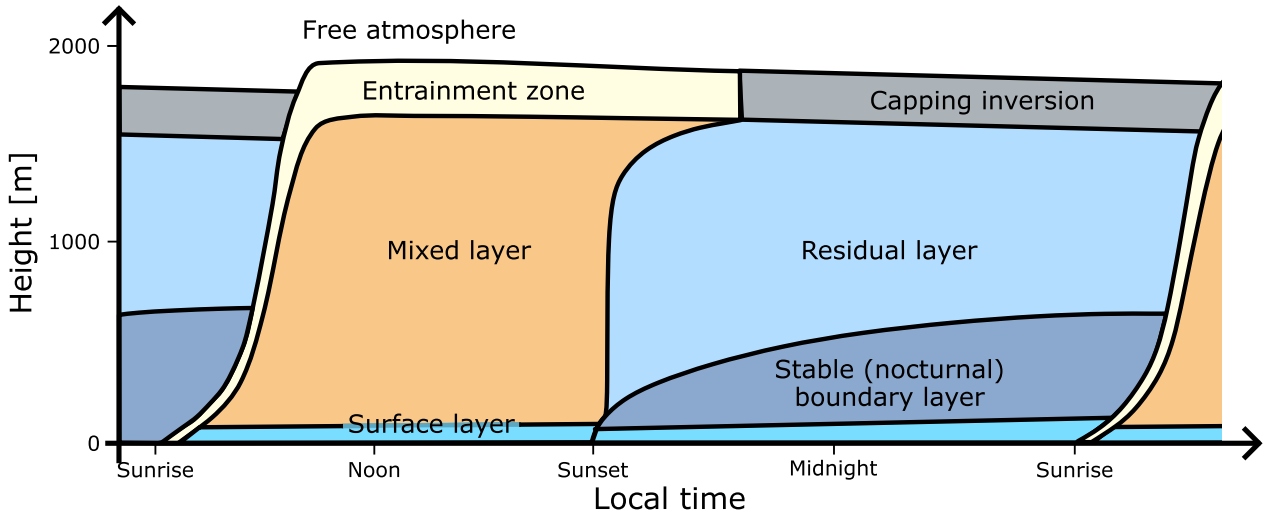

FIGURE 5. Schematic of atmospheric boundary layer diurnal variations (adapted from [57, p. 11]).

TABLE 4. Regression coefficients for the Sadot-Kopeika model in (31).

a_1	b_1	e
3.8×10^{-14}	2.0×10^{-15}	-5.3×10^{-13}
c_1	c_2	c_3
-2.8×10^{-15}	2.9×10^{-17}	-1.1×10^{-19}
d_1	d_2	d_3
-2.5×10^{-15}	1.2×10^{-15}	-8.5×10^{-17}

TABLE 5. Regression coefficients for the Sadot-Kopeika model in (32).

A_1	B_1	G
5.9×10^{-15}	1.6×10^{-15}	-3.9×10^{-13}
C_1	C_2	C_3
-3.7×10^{-15}	6.7×10^{-17}	-3.9×10^{-19}
D_1	D_2	D_3
-3.7×10^{-15}	1.3×10^{-15}	-8.2×10^{-17}
E_1	F_1	F_2
2.8×10^{-14}	-1.8×10^{-14}	1.4×10^{-14}

A second model is also suggested in [36] that offers improved performance when compared with the measurements. It extends the model in (31) by including the solar flux SF [Cal/cm^2/min] and the total cross-sectional area of particles per cubic meter TCSA [cm^2/m^3]. Indeed, the solar flux is expected to influence C_n^2 through its contribution to the temperature gradient. Particle scattering should not influence C_n^2 but it impacts the beam scintillation. Hence, the *effective* C_n^2 estimated from the measurements may include a contribution from the aerosol scattering [36]. With these new parameters, the model is

$$\begin{aligned} C_n^2 = {} & A_1 W + B_1 T + C_1 \mathrm{RH} + C_2 \mathrm{RH}^2 + C_3 \mathrm{RH}^3 \\ & + D_1 u_L + D_2 u_L^2 + D_3 u_L^3 + E_1 \mathrm{SF} \\ & + F_1 \mathrm{TCSA} + F_2 \mathrm{TCSA}^2 + G, \end{aligned} \tag{32}$$

with the different coefficients $A_1, B_1, \ldots, G$, given in Table 5.

Hence, this second Sadot-Kopeika model is of interest if the solar flux and the TCSA of particles are known. An estimation of the TCSA in [m^{-1}] from macroscale meteorological parameters at Beer-Sheva is available in [102] and [103]. It makes use of the following regression:

$$\begin{aligned} \mathrm{TCSA} = {} & \tilde{a}_1 \mathrm{RH} + \tilde{a}_2 \mathrm{RH}^2 + \tilde{a}_3 \mathrm{RH}^3 + \tilde{a}_4 \mathrm{RH}^4 + \tilde{a}_5 \mathrm{RH}^5 \\ & + \tilde{b} \ln(\mathrm{RH}) + \tilde{c}\, \mathrm{SF} + \tilde{d} \end{aligned} \tag{33}$$

where all coefficients $\tilde{a}_1, \tilde{a}_2, \ldots, \tilde{d}$, are given in Table 6, and $\ln(\cdot)$ is the natural logarithm.

TABLE 6. Regression coefficients for the TCSA model in (33).

$\tilde{a}_1$	$\tilde{a}_2$	$\tilde{a}_3$	$\tilde{a}_4$
9.69×10^{-4}	-2.75×10^{-5}	4.86×10^{-7}	-4.48×10^{-9}
$\tilde{a}_5$	$\tilde{b}$	$\tilde{c}$	$\tilde{d}$
1.66×10^{-11}	-6.26×10^{-3}	-1.34×10^{-5}	7.30×10^{-3}

The validation of the two Sadot-Kopeika models has been conducted with new measurements in the Negev desert in Sde-Boker (May 1990) and at Beer-Sheva (in winter time). Correlation coefficients between 0.86 and 0.92 were obtained [36].

Comments related to the coefficients given in Tables 4 and 5 can be found in the original paper [36]. The meteorological parameter ranges over which the regressions are valid are: from 9 to 35°C for the temperature, from 14 to 92% of relative humidity, and for wind speed between 0 and 10 m/s. Several

publications making use of the Sadot-Kopeika models are: [104], [105], [106].

b: BKB MODELS

The Bendersky-Kopeika-Blaunstein (BKB) models, referred to as BKB models in [107], extend Sadot-Kopeika models, namely by including the type of land through the albedo value A_l. They have been obtained from angle-of-arrival fluctuations along horizontal propagation paths, in the Negev desert and the Golan Heights (Israel) [108]. For temperatures ranging from 9 to 35°C, for wind speed values between 8 and 17 m/s, and for a relative humidity between 30 and 70%, the BKB daytime C_n^2 model gives C_n^2 at an altitude of 2.5 meter above ground from

$$C_n^2 = 3.8 \times 10^{-14} W + \frac{A_l}{e^T} 10^{-4} + f(u_L) + f(\mathrm{RH}) - 4.45 \times 10^{-14},$$

with W the temporal hour weight, as given in Table 3. For rocky terrain (rocky desert, Negev), an albedo value A_l equals to 0.35 is used, while the wind speed and humidity functions are [108]

$$f(u_L) = 8 \times 10^{-16} u_L - 4 \times 10^{-18} u_L^2,$$
$$f(\mathrm{RH}) = -8 \times 10^{-16} \mathrm{RH} + 5 \times 10^{-18} \mathrm{RH}^2.$$

For vegetation covered land (Golan), A_l is set to 0.5 and the functions $f(u_L)$ and $f(\mathrm{RH})$ are

$$f(u_L) = 2.58 \times 10^{-14} u_L$$
$$f(\mathrm{RH}) = -6.797 \times 10^{-15} \mathrm{RH}.$$

In case of nighttime and for vegetation covered land, the following model is suggested [108]

$$C_n^2 = 3 \times 10^{-17} T + 1.2 \times 10^{-14} u_L - 7.5 \times 10^{-16} \mathrm{RH} - 1.9 \times 10^{-14}, \quad (34)$$

that is only valid for 5 m/s $\leq u_L \leq$ 10 m/s and 92% $\leq$ RH $\leq$ 100%. The parametrization in (34) results from the observation that, in nighttime and for high relative humidity and wind speed values, the temporal hour weight W and the albedo value A_l slightly influence the ground C_n^2 value [108].

c: RYZNAR AND BARTLO MODEL

The Ryznar and Bartlo C_n^2 model is a regression of the wind speed u_L [m/s], measured at 10 meters, and of the solar irradiance SF [Cal/cm^2/min]. It is derived from scintillometer measurements (height of 4 meters) collected at the Boulder Atmospheric Observatory, CO, USA, and is given by [109]

$$C_n^2 = \left(0.12724 \times 10^{-6} + \check{b}_1 \mathrm{SF} + \check{b}_2 \mathrm{SF}^2 + \check{b}_3 \mathrm{SF}^3 + \check{c}_1 u_L + \check{c}_2 u_L^2 + \check{c}_3 u_L^3\right)^2, \quad (35)$$

with the regression coefficients in Table 7. The Ryznar and Bartlo model is valid for solar irradiance between 0.07 and 1.49 Cal/cm^2/min and wind-speed ranging from 0.3 to 19 m/s.

TABLE 7. Regression coefficients for the Ryznar and Bartlo model in (35).

$\check{b}_1$	$\check{b}_2$	$\check{b}_3$
0.17314×10^{-6}	0.62238×10^{-6}	-0.39727×10^{-6}
$\check{c}_1$	$\check{c}_2$	$\check{c}_3$
-0.33899×10^{-7}	0.10264×10^{-7}	-0.53824×10^{-9}

d: OTHER PARAMETRIZATIONS

Other models involving regressions of macroscale meteorological parameters can be found in the literature. For example, a recently published empirical C_n^2 model for communication links over a river can be found in [110]. It involves quantities such as the temperature difference between the air and the water, the dew point, as well as the ratio between the width of the river and the total length of the link. The Wang model [111] and the Raj model [112] are other examples, using similar meteorological quantities as the Sadot-Kopeika models.

Regressions involving ML approaches also exist in the recent literature and are detailed in Section V.

2) MONIN-OBUKHOV SIMILARITY THEORY MODELS

The description of boundary layers often relies on similarity theory, among which the Monin-Obukhov Similarity Theory (MOST) is well-known and used for modeling the atmospheric SL. Naturally, some ground C_n^2 models have been derived from MOST and this section presents the main relationships behind these models.

a: SIMILARITY THEORY

Similarity theory is based on BL experiments showing repeatable characteristics that cannot always be derived or explained from our current knowledge of physics. Instead, empirical relationships are established from these experiments, giving insights about BL processes by linking identified quantities of interests [57, p. 347].

Similarity theory starts thus with the identification of relevant (meteorological) quantities, or variables, to describe a given situation. They are then organized in dimensionless groups with the aid of the Buckingham Pi theorem, before conducting experiments in order to establish empirical relationships between groups. The hope is that, with appropriate dimensionless groups, universal relationships could be obtained. Similarity theory is often used in steady-state situations, i.e., not including time in the relevant variables, giving mean variables and turbulence statistics [57, p. 347].

b: MONIN-OBUKHOV SIMILARITY THEORY

MOST, also called surface-layer similarity, is applied to the atmospheric SL. In this layer, the fluxes of interest are the vertical momentum flux, the kinematic heat flux and the kinematic moisture flux [57, p. 52]. These fluxes are assumed constant in the SL and enable to define the friction velocity

u_*, the temperature scale θ_* (or T_*), and the humidity scale q_*, as given in [42].

From these scales, the Obukhov length L_{Ob} can be defined. Several definitions exist, depending on the choice of the temperature variable in the temperature scale: either the temperature T, or the potential temperature θ. In [57, p. 181], the Obukhov length definition is

$$L_{\text{Ob}} = \frac{-\bar{\theta}_v u_*^3}{k_a g(\overline{w'\theta'_v})_s},$$

with k_a the von Kármán constant ($k_a = 0.4$) and where $(\overline{w'\theta'_v})_s$ denotes the kinematic heat flux at the surface. A similar definition is used in [113], with the temperature T instead of the virtual potential temperature θ_v. In [42], L_{Ob} is given by

$$L_{\text{Ob}}^{-1} = \frac{g k_a}{u_*^2 \bar{T}} \left(T_* + \frac{0.61 \bar{T}}{\varrho + 0.61 \bar{q}} q_* \right), \tag{36}$$

with $\bar{T}$ and $\bar{q}$ representative values of the temperature and humidity in the surface layer, and ϱ the density of moist air.

Following MOST, any surface-layer meteorological quantity properly scaled by u_*, T_*, q_*, L_{Ob} and the height z, is a universal function of the stability parameter $\zeta = z/L_{\text{Ob}}$. For example, the vertical gradient of the average wind speed is given by [42]

$$\frac{\partial u_L}{\partial z} = \frac{u_*}{k_a z} \phi_m(\zeta), \tag{37}$$

where the similarity function $\phi_m(\zeta)$ is found empirically [42]

$$\phi_m(\zeta) = \begin{cases} (1 - 16\zeta)^{-1/4} & \text{for} \quad \zeta < 0 \quad \text{(unstable cond.)} \\ 1 + 7\zeta & \text{for} \quad \zeta > 0 \quad \text{(stable cond.)}, \end{cases}$$

for stable and unstable conditions (abbreviated cond.). Similarly, the vertical gradients of the average temperature and humidity are given by [42]

$$\frac{\partial T}{\partial z} = \frac{T_*}{k_a z} \phi_h(\zeta), \tag{38}$$

$$\frac{\partial q}{\partial z} = \frac{q_*}{k_a z} \phi_w(\zeta), \tag{39}$$

with

$$\phi_h(\zeta) = \phi_w(\zeta) = \begin{cases} (1 - 16\zeta)^{-1/2} & \text{for} \quad \zeta < 0 \quad \text{(unstable cond.)} \\ 1 + 7\zeta & \text{for} \quad \zeta > 0 \quad \text{(stable cond.)} \end{cases}.$$

Of particular interest for this work are the similarity functions associated with the SL temperature and humidity structure parameters C_T^2, C_q^2, and C_{Tq}. Their scaling is given in [42],

$$C_T^2 = \frac{T_*^2}{z^{2/3}} g_T(\zeta), \tag{40}$$

$$C_q^2 = \frac{q_*^2}{z^{2/3}} g_q(\zeta), \tag{41}$$

$$C_{Tq} = \frac{T_* q_*}{z^{2/3}} g_{Tq}(\zeta), \tag{42}$$

where $g_T(\zeta)$, $g_q(\zeta)$, and $g_{Tq}(\zeta)$ are similarity functions.[1] The expression of $g_t(\zeta)$ for C_T^2 is found in [113], and updated in [42]

$$g_T(\zeta) = \begin{cases} 4.9(1 - 6.1\zeta)^{-2/3} & \text{for} \quad \zeta \leq 0, \\ 4.9(1 + 2.2\zeta^{2/3}) & \text{for} \quad \zeta \geq 0. \end{cases} \tag{43}$$

This expression of $g_T(\zeta)$ is not unique and different numerical values are available in the literature [114].

Based on several experiments, detailed in [42], the similarity functions $g_T(\zeta)$, $g_q(\zeta)$, and $g_{Tq}(\zeta)$ are assumed to be equal. As a result,

$$\frac{z^{2/3} C_T^2}{T_*^2} = \frac{z^{2/3} C_q^2}{q_*^2} = \frac{z^{2/3} C_{Tq}}{T_* q_*} = g(\zeta),$$

where $g(\zeta) = g_T(\zeta) = g_q(\zeta) = g_{Tq}(\zeta)$. The refractive index structure parameter C_n^2 can then be obtained from [9, p. 172]

$$C_n^2 = \mathcal{A}^2 C_T^2 + \mathcal{B}^2 C_q^2 + 2\mathcal{A}\mathcal{B} C_{Tq}, \tag{44}$$

with $\mathcal{A} = \frac{\partial n}{\partial T}$ and $\mathcal{B} = \frac{\partial n}{\partial q}$, using (14) or (17) for the refractive index expression.

The SL C_n^2 follows thus the same similarity function $g(\zeta)$, and can be computed from measurements or estimations of T_*, q_* and L_{Ob}. Different approaches to obtain these required parameters are presented in the remainder of this section. More details about MOST can also be found in [116, p. 217] and [117].

c: BULK MODELS

Bulk models are based on the differences in mean values of meteorological parameters between two different heights (typically, a reference height and the surface) to estimate u_*, T_*, q_* and ζ [115]. Indeed, the integration of (37), (38) and (39), as conducted in [118] and [119], leads to [42], [114], and [115]

$$u_L(z) = \frac{u_*}{k_a} \left[\ln\left(\frac{z}{z_u}\right) - \Psi_m(\zeta) \right], \tag{45}$$

$$T(z) - T_s = \frac{T_*}{k_a} \left[\ln\left(\frac{z}{z_T}\right) - \Psi_h(\zeta) \right], \tag{46}$$

$$q(z) - q_s = \frac{q_*}{k_a} \left[\ln\left(\frac{z}{z_q}\right) - \Psi_w(\zeta) \right], \tag{47}$$

where T_s and q_s are the surface temperature and humidity, such that the left parts of (45) to (47) correspond to differences Δu_L, ΔT and Δq between a level z and the surface (the wind speed u_L is 0 at the surface), as anticipated for bulk models. The other side of the equality sign involves the roughness lengths of the wind speed z_u, of the temperature z_T, and of the humidity z_q. Those lengths are associated to the altitude levels where the different quantities u_L, T, and q, reach their surface values. Finally, the functions $\Psi_m(\zeta)$, $\Psi_h(\zeta)$, and $\Psi_w(\zeta)$ are the integrated forms of the functions

[1] In [114] and [115], a temperature-humidity correlation coefficient r_{Tq} is added to the expression of C_{Tq} given by (42), i.e., $C_{Tq} = r_{Tq} \frac{T_* q_*}{z^{2/3}} g_{Tq}(\zeta)$. It is often assumed to be equal to 0.8 under unstable conditions.

$\phi_m(\zeta)$, $\phi_h(\zeta)$, and $\phi_w(\zeta)$, respectively. More precisely, they correspond to the following integration, given for $\Psi_m(\zeta)$ for example,

$$\Psi_m(\zeta) = \int_0^{\zeta} \frac{1-\phi_m(\zeta')}{\zeta'} \mathrm{d}\zeta',$$

as explained in [118] and [119]. The analytical expressions resulting from the integration can be found in [114] and [119].

From (45) to (47), it should be possible to isolate u_*, T_* and q_*, that can then be fed in (40) to (42) and (44) to get C_n^2,

$$u_* = k_a\, u_L(z) \left[\ln\left(\frac{z}{z_u}\right) - \Psi_m(\zeta)\right]^{-1}, \tag{48}$$

$$T_* = k_a\, (T(z) - T_s) \left[\ln\left(\frac{z}{z_T}\right) - \Psi_h(\zeta)\right]^{-1}, \tag{49}$$

$$q_* = k_a\, (q(z) - q_s) \left[\ln\left(\frac{z}{z_q}\right) - \Psi_w(\zeta)\right]^{-1}. \tag{50}$$

From these equations, it seems that the knowledge of mean meteorological quantities at a level z and at the surface enables to find u_*, T_* and q_*. However, the roughness lengths z_u, z_T and z_q, are unknown, and usually parameterized as a function of u_*. Moreover, the stability parameter $\zeta = z/L_{Ob}$ itself is also dependent on u_*, T_* and q_*, as given in (36) for example. Hence, closed-form expressions for u_*, T_* and q_* are not possible.

To overcome this issue, two different approaches can be found in the literature:

1) The first approach is iterative, and aims at iteratively solving (45) to (47), with the definition of ζ and the parameterizations of the roughness lengths as given in [114] and the references therein. This is the approach presented in [114], [115], and [120], and recently applied in [121]. More details can also be found in [122].
2) The second approach starts from rewriting (48) to (50) with the drag coefficients c_D, c_T, and c_q [115]

$$u_* = c_D^{1/2} u_L(z),$$
$$T_* = c_T^{1/2}\, (T(z) - T_s),$$
$$q_* = c_q^{1/2} (q(z) - q_s).$$

From a theoretical point of view, the drag coefficients are simply equal to the expression they substitute, e.g., $c_D^{1/2} = k_a \left[\ln\left(\frac{z}{z_u}\right) - \Psi_m(\zeta)\right]^{-1}$. However, some empirical relationships have also been established and only depend on mean meteorological quantities [123]. Hence, closed-form expressions are possible in this case, as successfully applied in [124] and [125].

Finally, alternative approaches making use of two heights z_1 and z_2 instead of a reference height z and the surface have also been developed, such as the algorithm MARIAH [126], [127] or crude gradient approximations [113] for example. The Thiermann model is also based on MOST [111], [128], [129].

d: ARL MODEL

The American Army Research Laboratory (ARL) model, presented in [15], is inspired by MOST for obtaining C_n^2 in the SL. It involves some of the equations presented above for the bulk models, and requires only three measured parameters as inputs: the values of wind speed, temperature and C_n^2 at a single reference height. The determination of the stability conditions is also necessary, as well as the knowledge of the roughness length z_u. The procedure is then iterative to obtain u_*, T_* and L_{Ob}, and finally an SL C_n^2 profile. More details can be found in [11] and [15].

e: PAMELA MODEL

The PAMELA model is another model relying on MOST, described in several reports from the U.S. Naval Research Laboratory and the Army Research Laboratory [10], [130], [131], [132]. A complete description of the model is available in [10]. It makes use of (48) to compute the friction velocity u_*, where the roughness length is tabulated and depends on the surface conditions, while the Obukhov length is determined from the average wind speed at the roughness height (using the Pasquill stability parameter). Regarding the temperature scale T_*, it is estimated directly from the sensible heat flux H in [W/m^2] [10]

$$T_* = \frac{-H}{c_p \varrho u_*}, \tag{51}$$

with c_p the specific heat at constant pressure and ϱ the atmospheric density. An estimation of H is provided from the latitude, longitude, time of day, and cloud cover. As a result, the PAMELA model circumvents the need for an iterative solution.

f: KUNKEL AND WALTERS MODEL

The Kunkel and Walters model is also based on MOST [133] [9, p. 213]. By solving a time-dependent energy balance equation for the SL, it provides an estimation of the sensible and latent heat fluxes, that can then be used in MOST equations to get C_n^2. As inputs, this model requires the wind speed, the latitude, the time of the year, as well as some soil parameters and the soil moisture content. It assumes a clear sky (no cloud) and a surface with little vegetation, and has been validated with scintillometer measurements in New Mexico, USA [133].

g: NAVSLAM MODEL

The Navy Vertical Surface Layer Model (NAVSLaM) is another example of surface C_n^2 model based on MOST to model OT in maritime environments [134], [135]. As inputs, it requires measured or modeled meteorological quantities (wind speed, air temperature, and humidity) in the atmospheric SL, at one or two height levels.

h: USE OF NUMERICAL WEATHER PREDICTION SOFTWARE

Current NWP software can embed a MOST-based description of the BL, as well as other parametrizations involving a

variety of turbulence closure models. By using such software to model macroscale meteorological quantities, alternative quantities can be retrieved in the BL, e.g., the TKE, the friction velocity, kinematic fluxes, etc. As a result, from a user point-of-view, the BL quantities predicted by the software can be plugged in the equations presented above to retrieve the ground C_n^2 value.

This approach is illustrated in [136] for example, where surface fluxes and roughness lengths are extracted from the weather simulations to predict local C_n^2 at the surface. A similar approach is used in [101] and [137], where the friction velocity u_*, the sensible latent heat flux H and the latent heat flux E are retrieved from NWP simulations and linked to the turbulent fluxes.

B. ATMOSPHERIC BOUNDARY LAYER

Modeling of the atmospheric BL is challenging and depends on the stability. Usually, unstable and free convective conditions occur during daytime, while stable conditions are found in nighttime. Nevertheless, these simple rules are sensitive to the local conditions and may not apply to all locations. For example, snow-covered terrains with warm air over cold ground experience stable conditions during daytime. As a result, it is advised to rely on the potential temperature lapse rate when concluding about local stability condition [9, p. 213].

According to [109, p. 13] and numerous works referenced therein, height variations of C_T^2 and C_n^2 in the atmospheric BL fit within the framework of MOST, giving an altitude dependency in $z^{-4/3}$ of C_T^2 for unstable conditions, while stable conditions lead to a dependency in $z^{-2/3}$. C_n^2 is then assumed to follow the same altitude dependency as C_T^2 [99], or can be derived from (44).

The following of this section presents some BL C_n^2 models based on these two trends: $z^{-4/3}$ in daytime and $z^{-2/3}$ in nighttime. Such results are often found in the literature, for example in [15, p. 14], [4, p. 480], [9, p. 213], etc.

1) CONVECTIVE BOUNDARY LAYER (DAYTIME)

Two common models used for describing C_n^2 in the convective (unstable) BL are the Kaimal model and the Kukharets and Tsvang model [9, p. 214], [15, p. 20], [109, p. 14]. Both include a $z^{-4/3}$ dependency that inspired the BL term in the HAP model presented in Section III-A4. They provide profiles for average turbulence conditions at the locations where they have been developed.

a: KAIMAL MODEL

The Kaimal model has been developed based on C_T^2 measurements in the BL in New Mexico, USA [138]. It originally made use of the surface heat flux but has been later extended to rely on the knowledge of C_T^2 (or C_n^2) at a given altitude near the ground [99]. The Kaimal model expressed in terms of C_T^2 can be found in [15, p. 20], while its C_n^2-based form assuming that C_n^2 has the same dependency as C_T^2 is given by [99] and [109, p. 16]

$$\frac{C_n^2(z)}{C_n^2(z_0)} = \begin{cases} \left(\frac{z}{z_0}\right)^{-4/3} & \text{for } z_0,\, z \le 0.5 z_i, \\ \left(\frac{0.5 z_i}{z_0}\right)^{-4/3} & \text{for } 0.5 z_i \le z \le 0.7 z_i, \\ 2.9 \left(\frac{0.5 z_i}{z_0}\right)^{-4/3} \left(\frac{z}{z_i}\right)^{3} & \text{for } 0.7 z_i \le z \le z_i, \end{cases}$$

where z_0 is the near-ground altitude where C_n^2 is known (e.g., measured), and z_i is the altitude of the inversion layer, associated to the top of the atmospheric BL. Three segments can be identified: the mixed layer up to $0.5\, z_i$ where C_n^2 scales as $z^{-4/3}$, a transition layer where C_n^2 is constant, and an interface layer between the BL and the troposphere.

Extensions of the Kaimal model have been developed in the High Energy Laser Handbook Empirical Model (HELHEM) for example [15, p. 20].

b: KUKHARETS AND TSVANG MODEL

The Kukharets and Tsvang model also applies to convective BLs and has been derived from measurements in the Soviet Union, over steppe and forested surfaces [139]. In comparison with the Kaimal model, it enables to represent increased turbulence arising at the top of the BL using a Gaussian shape in the profile. Moreover, it avoids the segmentation of the profile in different regions.

The Kukharets and Tsvang model has initially been presented in terms of $C_T^2(\xi)$, where $\xi = z/z_i$ is a normalized altitude, with z_i identified as the height where an abrupt decrease in the turbulence energy dissipation rate is observed. The main equation of the model is [109, p. 16]

$$\frac{C_T^2(\xi)}{C_T^2(0.1)} = k_1\, \xi^{-4/3} + k_2\, \mathrm{e}^{-k_3(\xi-1.1)^2},$$

with $k_1 = 0.046$, $k_2 = 0.6$ and $k_3 = 12$. Hence, the C_T^2 profile is normalized with C_T^2 at an altitude $z/z_i = 0.1$. It has a $z^{-4/3}$ variation for altitudes below z_i, and a Gaussian-shaped layer at altitude z_i which magnitude is given by k_2 and standard deviation influenced by k_3.

The model has later been modified in [140] to allow for any reference altitude, and applied to C_n^2. The updated model is [140] [9, p. 215]

$$\frac{C_n^2(z)}{C_n^2(z_0)} = \frac{k_1 \left(\frac{z}{z_i}\right)^{-4/3} + k_2\, \mathrm{e}^{-k_3\left(\frac{z}{z_i}-1.1\right)^2}}{k_1 \left(\frac{z_0}{z_i}\right)^{-4/3}}.$$

In [15, p. 21], the model has been further modified to account for measurements taken in a desert basin (New Mexico) [141], while removing the $z^{-4/3}$ trend above the inversion layer:

$$\log_{10}(C_T^2(z)) = \log_{10}(C_T^2(0)) + 0.775\, \mathrm{e}^{-\frac{(z-0.95\, z_i)^2}{2(z_i/7)^2}} + \left(\frac{1}{3} + \frac{4}{3}\log_{10}\left(\frac{z}{z_i}\right)\right) \cdot \sigma\left(\frac{z_i - z}{z_i/8}\right),$$

where $\sigma(z) = \frac{1}{1+e^z}$, such that $\lim_{z\to\infty}\sigma(z) = 0$ and $\lim_{z\to-\infty}\sigma(z) = 1$. $C_T^2(0)$ is the surface C_T^2 value, as given by a MOST-based model for example.

2) STABLE BOUNDARY LAYER (NIGHTTIME)

Fewer models are available for describing the altitude dependency of C_n^2 in stable atmospheric BLs. This may be explained by the lack of profile measurements in this layer. Moreover, energy sources responsible for atmospheric turbulence are smaller in the absence of convection (e.g., wind driven mixing, gravity waves), hence less predictable and more localized [15, p. 38].

From MOST, a $z^{-2/3}$ trend is expected in the SL but does not seem to extend very far in the BL. Decreases lower than $z^{-2/3}$ have been suggested in the literature [113], [109, p. 17], as well as a "z-less" dependency for altitudes larger than L_{Ob}, only associated to the local wind and temperature gradients at each level [142], [15, p. 38]. A large range between $z^{-0.5}$ and z^{-2} has also been observed but requires further validation [109], [9, p. 217].

Nevertheless, nighttime BL C_n^2 profiles are of particular interest for astronomical observations. According to [68] and based on 168 radiosonde flights taken during nighttime at nine astronomical sites, the mean and median profiles in the BL, assumed to extend from 0 to 1 km above the surface, are given by

$$C_{n_{\text{median}}}^2(z) = 1.39 \times 10^{-13}\, z^{-1.45},$$
$$C_{n_{\text{mean}}}^2(z) = 1.24 \times 10^{-12}\, z^{-1.53}.$$

The altitude dependency and amplitude of these profiles have been fitted based on the measurements, and question the validity of the $z^{-2/3}$ trend, or the stability conditions of the BL.

V. MACHINE LEARNING-BASED C_N^2 MODELS

In recent years, ML has developed considerably, driven by new advances in computational resources and the abundance of data that can be collected and processed. ML refers to computer systems able to learn and improve based on data they process, without following explicit instructions from a programmer. It can be applied to diverse fields of human knowledge, and science has seen an increase in ML-based models. This is also the case of C_n^2 modeling and this section presents some of the new models published in the past 5 to 10 years,[2] as well as highlighting the motivations behind ML approaches.

A. OVERVIEW OF MODELS

Focus is given here to ML models directly providing C_n^2 from meteorological quantities, either for surface C_n^2 (Section V-A1) or for vertical C_n^2 profiles (Section V-A2).

[2]The list is not exhaustive but presents the main approaches used for ML-based C_n^2 models.

1) SURFACE C_N^2 MODELS

Several ML-based C_n^2 models for ground (surface) C_n^2 are available, generalizing or complementing the models presented in Section IV. They usually rely on simultaneous measurements of surface meteorological parameters and C_n^2 in order to learn (non)linear relationships between them.

One of the pioneering model is the Wang and Basu model, published in 2016 [143]. It uses a multilayer perceptron artificial neural network with only one hidden layer to predict ground C_n^2 time series based on five variables: 2-meter temperature, 2-meter relative humidity, 2-meter pressure, 15-meter potential temperature gradient and 15-meter wind shear. The model has been trained with and validated on data at Mauna Loa Observatory, Hawaii (USA), capturing the temporal evolution of ground C_n^2 and enabling its prediction in very stable conditions. The application of this model and its extension to Antarctica are given in [144]. A similar approach is used in [145] to predict the integrated C_n^2 in the SL at Paranal Observatory.

Various ML models have been explored in [146] and showed improvements by including the solar flux as an input. Performance is also improved when giving the Wyngaard model predicted C_n^2 as an input to the ML algorithms.

Other ML models have been presented in [147], [148], [149], and [150], comparing the performance with the NAVSLaM model in maritime environments. The models in [148] use the following macroscopic meteorological parameters as inputs: wind speed and direction, air temperature, air pressure, relative humidity, solar radiation, dew point and rainfall rate. A classifier between weak and strong turbulence is also introduced.

In [151], twelve different input quantities are given to the ML models in order to predict surface C_n^2 in a near-maritime environment. The relative importance of the inputs has been established, suggesting that air temperature, pressure, air-water temperature difference, temporal hour weight and time of the year are important parameters to accurately predict C_n^2. The model is further extended in [152] and compared with regression-based approaches (see Section IV-A1).

It is worth highlighting that the use of ML does not prevent access to analytical expressions. Indeed, in [153], a group method of data handling neural network is presented to predict surface C_n^2 at the Baikal Astrophysical Observatory, providing "learned" analytical equations. These equations involve various powers of the ground temperature, wind speed, pressure and humidity.

Finally, hybrid models have been introduced, namely in [154]. They rely on a macro-meteorological model, similar to the ones presented in Section IV-A1, and referred to as the baseline model in [154]. Then, an ML model is trained on the baseline model residual errors, i.e., the differences between the baseline model predictions and the actual measurements, in order to learn and correct those errors. This approach can be of particular interest to include local effects and learn features specific to a given environment, while using a baseline model validated at another location.

2) C_N^2 PROFILE MODELS

The ML algorithms for obtaining C_n^2 profile models are similar to the algorithm presented for surface C_n^2. They involve macroscale meteorological parameters, with the altitude z added as an input to the ML algorithm. This is the case for the neural networks presented in [155] and [156] for example, validated with C_n^2 profile measurements over the Tibetan Plateau and in a marine environment (Haikou, China). A comparable approach is presented in [157], focussing only on the BL profile.

Alternatively, models combining ML approaches and physical models have been developed, such as the MEP approach from [80], presented in Section III-B5.

B. MOTIVATIONS FOR MACHINE LEARNING-BASED MODELS

Based on the various ML-based references consulted, several motivations behind the use of ML models to predict C_n^2 can be highlighted.

1) SITE DEPENDENCY

For the moment, ML approaches are rather site-specific, as they are trained based on measurements collected at a given location. However, the architecture of ML models (e.g., the choice of using a neural network with a given number of layers and requiring specified macro-meteorological quantities as inputs) is generic and can easily be applied to new measurements at other locations. Hence, provided that local measurements are available, an ML model can easily be (re)trained to provide accurate predictions at this location.

Furthermore, in the future, location-agnostic models could be developed, if trained with large amounts of data coming from various environments [149].

2) HYBRID MODELS

Relying on ML does not necessarily imply to get rid of all C_n^2 models developed in the past and based on empirical observations of physical insights. Indeed, hybrid models, as introduced in [154], are useful to combine ML with other "classical" C_n^2 models, while the outputs of "classical" models can also be used as inputs to ML models [146].

3) MODEL EXTENSIONS

Some of the models presented in this chapter rely on hypotheses that may not be fulfilled, e.g., unstable conditions. On the contrary, with appropriate training in all conditions, ML models can circumvent this issue [143].

4) PHYSICAL INSIGHTS

Last but not least, ML models can provide physical insights about the underlying processes by identifying the most important features and input parameters. This is illustrated in [158], where various non-dimensional groups are constructed based on surface meteorological parameters prior to using an ML approach. Then, groups leveraging the most accurate predictions can be identified, as well as the relevant input parameters.

VI. CONCLUSION

This paper presents a comprehensive and detailed review of the various C_n^2 models available in the literature, including models developed in the 1970s and still widely used today (e.g., Hufnagel-Valley models). There is ongoing development of new models, namely using ML approaches, for different sites, seasons, and applications.

This literature review highlights the key parameters commonly used in C_n^2 models, such as temperature gradients and wind shear, which significantly influence atmospheric turbulence. It also emphasizes the necessity of carefully handling the BL to capture its diurnal variations. Furthermore, it shows that several literature-based C_n^2 models only provide average or median C_n^2 profiles, derived from measurements at a single location. They are therefore not suited for depicting localized OT layers, which are expected to induce most of OT and vary with time [79], [159].

In addition to the factual observations and conclusions given above, our views on ideal C_n^2 models suited for optical communication applications are:

- location- and seasons-independent models, such that the same model can be applied to different locations and at various times, yielding access to local and instantaneous C_n^2 profiles;
- models relying on large-scale meteorological quantities, that can be easily obtained;
- models avoiding excessive empiricism, or that allow for easy site-specific calibration.

Such ideal models, falling into the category of parametric models, could potentially incorporate inputs from NWP or make use of ML approaches. Hybrid models that separately address the FA and the BL also show significant promise [160], [161].

Nevertheless, any C_n^2 model applied to FSOC must be properly validated with measurement campaigns conducted at the sites of interest, exploiting multiple metrics for the comparison, as detailed in Appendix A.

APPENDIX A
METRICS FOR C_N^2 PROFILE COMPARISONS

In this work, many models for C_n^2 profiles have been introduced. The validity and quality of these models depend on their agreement with measurements and observations of C_n^2 profiles. In the literature, different metrics have been suggested in order to quantitatively evaluate the agreement between models and measurements, and are summarized in this section. The wording used always refers to a modeled profile and a measured one, but the metrics could also be used to compare profiles directly coming from different models (i.e., substituting "measured profiles" by "profiles coming from another model"). Some metrics have initially been suggested to compare vertical profiles of meteorological quantities, such as temperature, pressure, wind speed, etc., and then been applied for comparing C_n^2 profiles.

A. COMMON STATISTICAL METRICS

Most statistical metrics can be used with vertical profiles of any quantities (e.g., temperature profiles $T(z)$, C_n^2 profiles, etc.). Hence, the following notations are introduced: $X(z)$ refers to the observed profile of a specified quantity (T, C_n^2, etc.), while $Y(z)$ denotes the modeled profile of the same quantity. Since several observations are usually collected at a given location for different times, an index i is added to refer to the i-th observation, i.e., $X_i(z)$. Similarly, the modeled profile corresponding to this observation is $Y_i(z)$. Averaging can then be conducted over the different observations i, with N_{obs} being the total number of collected observations.

For C_n^2 profile comparisons, $X(z)$ and $Y(z)$ are very often chosen as the logarithms in base 10 ($\log_{10}$) of measured and modeled C_n^2, given that C_n^2 can span several orders of magnitude. It is often required for $X(z)$ and $Y(z)$ to have the same vertical sampling for the altitudes. If it is not the case, reinterpolation of the individual profiles can be used.

1) MEAN, VARIANCE AND STANDARD DEVIATION PROFILES

From a set of measured vertical profiles $\{X_i(z)\}_{1,\dots,N_{\text{obs}}}$, the *average (or mean) measured profile* $\bar{X}(z)$ is given by

$$\bar{X}(z) = \frac{1}{N_{\text{obs}}} \sum_{i=1}^{N_{\text{obs}}} X_i(z). \tag{52}$$

Similarly, the *average (or mean) modeled profile* $\bar{Y}(z)$ coming from a set of modeled profiles $\{Y_i(z)\}_{1,\dots,N_{\text{obs}}}$ is computed.

Fluctuations around the average profiles are measured by the *variance profiles* $\sigma_X^2(z)$ and $\sigma_Y^2(z)$, where $\sigma_X(z)$ is the *standard deviation (std)* profile of the measured profiles, while $\sigma_Y(z)$ is the one associated to the modeled profiles. For instance, $\sigma_X^2(z)$ is computed using

$$\sigma_X^2(z) = \frac{1}{N_{\text{obs}} - 1} \sum_{i=1}^{N_{\text{obs}}} \left(X_i(z) - \bar{X}(z)\right)^2.$$

In cases where the logarithm of C_n^2 is used for $X_i(z)$ and $Y_i(z)$, e.g., $\log_{10}(C_n^2(z))$, the mean computed from (52) tends to the median profile of C_n^2 [9, p. 218]. This follows the assumption of a log-normal distribution for C_n^2, as briefly introduced in the next paragraph.

2) MEDIAN, QUARTILES AND DISTRIBUTIONS

Based on multiple samples of C_n^2 profiles, the *distributions* of possible C_n^2 values at a given altitude can be computed. The *median profile* can then be obtained, as well as any *quartile profile*. For example, in [162], the median, first quartile, and third quartile profiles are computed and compared between the measured and modeled C_n^2 profiles.

In [95], the distributions are obtained for C_T^2, for four different parts of the atmosphere (BL, troposphere, tropopause, and stratosphere). It is shown that the logarithm in base 10 of C_T^2, normalized by its median value, follows a Gaussian distribution (chi-square test, estimation of skewness and kurtosis). As a result, C_T^2 (and equivalently, C_n^2) is distributed according to a log-normal distribution, and the average of $\log_{10}(C_n^2)$ tends to the median values.

3) BIAS, RMSE AND BIAS-CORRECTED RMSE

The definitions of the bias, Root-Mean-Square Error (RMSE) and bias-corrected RMSE presented below are inspired from, and used in, [50], [53], [163], [164], and [165].

Given the sets of measured vertical profiles $\{X_i(z)\}_{1,\dots,N_{\text{obs}}}$ and modeled profiles $\{Y_i(z)\}_{1,\dots,N_{\text{obs}}}$, the *bias*, also named *Mean Bias Error (MBE)* in [92], is defined as

$$\text{BIAS}(z) = \frac{1}{N_{\text{obs}}} \sum_{i=1}^{N_{\text{obs}}} \left(Y_i(z) - X_i(z)\right) = \bar{Y}(z) - \bar{X}(z). \tag{53}$$

In (53), the altitude dependency of the bias is made explicit, since it is indeed a vertical profile of the bias that is obtained. The *absolute bias*, or *Mean Absolute Error (MAE)*, has a similar definition, except that the absolute value of the error (i.e., the difference between the modeled and the measured profiles) is used,

$$\text{ABSOLUTE BIAS}(z) = \frac{1}{N_{\text{obs}}} \sum_{i=1}^{N_{\text{obs}}} \left|Y_i(z) - X_i(z)\right|. \tag{54}$$

Similarly, the *RMSE* profile is defined by

$$\text{RMSE}(z) = \sqrt{\frac{1}{N_{\text{obs}}} \sum_{i=1}^{N_{\text{obs}}} \left(Y_i(z) - X_i(z)\right)^2}. \tag{55}$$

The bias enables to identify systematic errors between the models and the measurements, while the RMSE includes systematic and statistical errors. To remove the systematic error from the RMSE, the *bias-corrected RMSE*, also named *centred RMSE* in [50], is used, given by

$$\begin{aligned}\text{CRMSE}(z) &= \sqrt{\frac{1}{N_{\text{obs}}} \sum_{i=1}^{N_{\text{obs}}} \left[\left(Y_i(z) - \bar{Y}(z)\right) - \left(X_i(z) - \bar{X}(z)\right)\right]^2} \\ &= \sqrt{\frac{1}{N_{\text{obs}}} \sum_{i=1}^{N_{\text{obs}}} \left[\left(Y_i(z) - X_i(z)\right) - \left(\bar{Y}(z) - \bar{X}(z)\right)\right]^2} \\ &= \sqrt{\text{RMSE}^2(z) - \text{BIAS}^2(z)}.\end{aligned}$$

These metrics are very often used, also for comparing profiles of meteorological quantities. In the case of wind direction, slight modifications are necessary to account for its periodicity (angular direction), as stated in [166].

4) VERTICAL AVERAGING

The error metrics previously defined in this section, i.e., the (absolute) bias, RMSE and bias-corrected RMSE, are profiles of the altitude. In order to reduce them to single scalar values, averaging over the altitudes is sometimes conducted, considering that discrete sampled altitudes $\{z_m\}_{m=1,\dots,N_s}$ are available [83]. For example, the altitude-averaged bias is

$$\overline{\text{BIAS}} = \frac{1}{N_s} \sum_{m=1}^{N_s} \text{BIAS}(z_m) = \frac{1}{N_s} \sum_{m=1}^{N_s} \text{BIAS}(m\Delta z), \tag{56}$$

with N_s the number of sampled altitudes and Δz the sampling distance between the altitudes (assumed constant, i.e., $z_m = m\Delta z$). Equation (56) can be generalized for the other metrics.

The main drawback of altitude-averaging is the loss of information about the profile that enables to determine which part of the atmosphere are better (or worse) modeled. However, this could be mitigated by averaging for different parts of the atmosphere, for example for the ground layer, the troposphere, and the stratosphere [91]. In this case, three scalar values summarize the profile metrics.

As a complementary remark, some references conduct the averaging only on the altitudes and not over a set of different measured profiles. Hence, one scalar metric per observed profiles is obtained [50], [51], e.g.,

$$\text{BIAS}_i = \frac{1}{N_s}\sum_{m=1}^{N_s}\left(Y_i(m\Delta z) - X_i(m\Delta z)\right).$$

5) RELATIVE ERRORS

The error between the measured $X_i(z)$ and the modeled $Y_i(z)$, as used in (53) and (54), can be divided by the measured value $X_i(z)$ in order to obtain the relative error. It is then averaged over the multiple sampled profiles, yielding the *average (absolute) relative error profile* [91]. It is referred to as the *Mean Relative Error (MRE)* in [92], defined by

$$\text{MRE}(z) = \frac{1}{N_{\text{obs}}}\sum_{i=1}^{N_{\text{obs}}}\frac{|Y_i(z) - X_i(z)|}{|X_i(z)|}.$$

Averaging over different atmospheric regions can then be performed [91].

6) CORRELATION COEFFICIENTS

Correlation coefficients R_{XY} measure statistical relationships between two variables. The *Pearson correlation coefficient*, noted R_{XY}, measures the linear relationship between the variables, and is defined as the ratio between the covariance of the two variables and the product of their standard deviation.

An altitude profile of the correlation coefficient could be defined as

$$\begin{aligned} R_{XY}(z) &= \frac{\sigma_{XY}(z)}{\sigma_X(z)\,\sigma_Y(z)} \\ &= \frac{\sum_{i=1}^{N_{\text{obs}}}\left(X_i(z) - \bar{X}(z)\right)\left(Y_i(z) - \bar{Y}(z)\right)}{\sqrt{\sum_{i=1}^{N_{\text{obs}}}\left(X_i(z) - \bar{X}(z)\right)^2}\sqrt{\sum_{i=1}^{N_{\text{obs}}}\left(Y_i(z) - \bar{Y}(z)\right)^2}} \end{aligned}$$

where $\sigma_{XY}(z)$ is the covariance profile between $X(z)$ and $Y(z)$, i.e.,

$$\sigma_{XY}(z) = \frac{1}{N_{\text{obs}} - 1}\sum_{i=1}^{N_{\text{obs}}}\left(X_i(z) - \bar{X}(z)\right)\left(Y_i(z) - \bar{Y}(z)\right).$$

In practice, the correlation coefficient is averaged over the altitudes to get one scalar value, using

$$\overline{R}_{XY} = \frac{1}{N_s}\sum_{m=1}^{N_s} R_{XY}(m\Delta z).$$

Alternatively, the coefficient can be averaged over only a given part of the atmosphere, as in [92].

Finally, in [51], the coefficient is computed for each measured profile, averaging over the altitudes:

$$R_{XY,i} = \frac{\sum_{m=1}^{N_s}\left(X_i(m\Delta z) - \bar{X}_i\right)\left(Y_i(m\Delta z) - \bar{Y}_i\right)}{\sqrt{\sum_{m=1}^{N_s}\left(X_i(m\Delta z) - \bar{X}_i\right)^2}\sqrt{\sum_{m=1}^{N_s}\left(Y_i(m\Delta z) - \bar{Y}_i\right)^2}},$$

with $\bar{X}_i$ (resp. $\bar{Y}_i$) the altitude-average of the i-th measured (resp. modeled) profile.

B. ALTERNATIVE METRICS

In addition to the common statistical metrics presented above, custom metrics are sometimes used for comparing C_n^2 profiles. Some of them are presented in this section.

1) RELATIVE ERROR OF INTEGRATED C_N^2

In [95], the relative error of the integrated C_n^2 over 1 km thick layers is defined, noted EIC_n^2. As this metric is computed for each pair of measured and modeled profiles, it can be indexed by i, using the notations introduced previously. Hence, for a layer centred at an altitude z_m (in meter) and for the i-th measured/modeled profile, its $\text{EIC}_{n,i}^2(z_m)$ is defined by

$$\begin{aligned} &\text{EIC}_{n,i}^2(z_m) \\ &= \frac{\left|\log_{10}\left(\int_{z_m-500}^{z_m+500} Y_i(z)\,\text{d}z\right) - \log_{10}\left(\int_{z_m-500}^{z_m+500} X_i(z)\,\text{d}z\right)\right|}{\log_{10}\left(\int_{z_m-500}^{z_m+500} X_i(z)\,\text{d}z\right)}, \end{aligned}$$

where $X_i(z)$ is the i-th measured C_n^2 profile, and $Y_i(z)$ is the associated modeled C_n^2 profile. The logarithm is taken after the integration, $X_i(z)$ and $Y_i(z)$ are thus directly the C_n^2 values and not their logarithms. As a generalization, the width of the layer, i.e., the bounds for the integration over the altitudes, can be modified.

The average profile of the relative errors of integrated C_n^2, computed over all profiles indexed by i, estimates the static error of the models, while its standard deviation shows the gain of reliability in C_n^2 profile prediction from the models [95].

2) INDEX OF AGREEMENT

Inspired by [167] and the references therein, [92] makes use of the statistical index of agreement IoA to compare measured and modeled profiles of meteorological quantities. It is defined by

$$\text{IoA}(z) = 1 - \frac{\sum_{i=1}^{N_{\text{obs}}}\left(Y_i(z) - X_i(z)\right)^2}{\sum_{i=1}^{N_{\text{obs}}}\left(|Y_i(z) - \bar{Y}(z)| - |X_i(z) - \bar{X}(z)|\right)^2},$$

and varies between 0 (total disagreement) and 1 (perfect agreement). Alternative definitions as well as more explanations behind the origin of this index can be found in [167]. A weighted (linear) combination of indexes of agreement for several meteorological quantities in order to define a new merit function is also introduced in [92].

3) CUSTOMIZED FIGURES OF MERIT

If deemed relevant, any metric presented previously can be combined to define a custom figure of merit. For example, a simple linear combination can be made, or more complex

expressions can be used (e.g., see the definition of the index of agreement).

C. INTERESTS OF MULTIPLE METRICS

The various metrics presented are useful to validate developed models with real observations. Furthermore, they can also be of interest to get insights about the model parameters, e.g., by monitoring the evolution of the metrics when tuning some parameters of the models. It is always a good practice to monitor several metrics to assess the quality of a model and use them in a complementary way.

REFERENCES

[1] F. Quatresooz, G. O. D. Xivry, O. Absil, D. Vanhoenacker-Janvier, and C. Oestges, "Challenges for optical turbulence characterization and prediction at optical communication sites," *Proc. SPIE*, vol. 12777, pp. 2410–2424, Jul. 2023.

[2] V. I. Tatarskii, "The effects of the turbulent atmosphere on wave propagation," *Jerusalem, Isr. Program Sci. Translations*, Dec. 1972. [Online]. Available: https://ui.adsabs.harvard.edu/abs/1971etaw.book.....T/abstract

[3] F. Roddier, "V the effects of atmospheric turbulence in optical astronomy," in *Progress in Optics*, vol. 19. Amsterdam, The Netherlands: Elsevier, 1981, pp. 281–376.

[4] L. C. Andrews and R. L. Phillips, "Laser beam propagation through random media," in *Laser Beam Propagation Through Random Media*, 2nd ed., Washington, DC, USA: SPIE, 2005.

[5] R. Griffiths, K. E. Hartley, J. Osborn, O. J. D. Farley, R. W. Wilson, M. Townson, L. Beesley, A. Rodriguez-Gomez, A. Comeron-Tejero, and D. Alaluf, "TURBO: An automatic 24-hour turbulence monitoring station in Barcelona," in *Proc. Int. Conf. Space Opt.*, Aug. 2024, p. 300.

[6] A. Ziad, C. Giordano, A. Aresta, E. Aristidi, C. Bailet, F. Berto, C. Bertolin, M. Carbillet, S. Cavazzani, D. Ceus, and T. Charbonnel, "ANATOLIA: A high-performance mobile station for atmospheric characterization for astronomical observations and optical communications," in *Adaptive Optics for Extremely Large Telescopes*, 7th ed., 2023. [Online]. Available: https://hal.science/hal-04402830/document

[7] L. Paillier, Y. Lai-Tim, A. Poiron, E. Klotz, S. Lefebvre, C. Musso, T. Fusco, C. Petit, A. M. Bonnefois, E. Chalali, K. Caillault, L. Hespel, L. Krafft, J. Montri, F. Quatresooz, S. Poulenard, and N. Véedrenne, "Propagation channel assessment for GEO feeder links," in *Proc. IEEE Int. Conf. Space Opt. Syst. Appl. (ICSOS)*, Oct. 2023, pp. 93–102.

[8] R. E. Good, R. R. Beland, E. A. Murphy, J. H. Brown, and E. M. Dewan, "Atmospheric models of optical turbulence," *Proc. SPIE*, vol. 928, pp. 165–186, Aug. 1988.

[9] R. B. Robert, "Propagation through atmospheric optical turbulence," *Atmos. Propag. Radiat.*, vol. 159, pp. 157–232, Jan. 1993.

[10] J. C. Ricklin, S. M. Hammel, F. D. Eaton, and S. L. Lachinova, "Atmospheric channel effects on free-space laser communication," *J. Opt. Fiber Commun. Rep.*, vol. 3, no. 2, pp. 111–158, Apr. 2006.

[11] L. Canuet, "Atmospheric turbulence profile modeling for satellite-ground laser communication," M.S. thesis, Univ. Politècnica de Catalunya, Barcelona, Spain, 2014. [Online]. Available: https://upcommons.upc.edu/handle/2117/86039

[12] M. Miller and P. Zieske, *Turbulence Environment Characterization*. Everett, MA, USA: Defense Advanced Research Projects Agency, 1978. [Online]. Available: https://apps.dtic.mil/sti/citations/ADA072379

[13] M. C. Roggemann, B. M. Welsh, and B. R. Hunt, *Imaging Through Turbulence*. Boca Raton, FL, USA: CRC Press, 1996.

[14] R. R. Parenti and R. J. Sasiela, "Laser-guide-star systems for astronomical applications," *J. Opt. Soc. Amer. A, Opt. Image Sci.*, vol. 11, no. 1, pp. 288–309, 1994.

[15] D. H. Tofsted, S. G. O'Brien, and G. T. Vaucher, "An atmospheric turbulence profile model for use in army wargaming applications I," U.S. Army Res. Lab., White Sands Missile Range, NM, USA, Tech. Rep. ARL-TR-3748, Feb. 2006.

[16] D. P. Greenwood, "Bandwidth specification for adaptive optics systems," *J. Opt. Soc. Amer.*, vol. 67, no. 3, pp. 390–393, Mar. 1977.

[17] A. Gurvich and M. Gracheva, "Simple models of turbulence," *Izv. Akad. Nauk SSSR, Fiz. Atmos. Okeana*, vol. 16, pp. 1107–1111, Jan. 1980.

[18] A. J. MacGovern, D. A. Nahrstedt, and M. M. Johnson, "Atmospheric propagation for tactical directed-energy applications," *Proc. SPIE*, vol. 4034, pp. 128–139, Jul. 2000.

[19] J. L. Bufton, "Comparison of vertical profile turbulence structure with stellar observations," *Appl. Opt.*, vol. 12, no. 8, pp. 1785–1793, 1973.

[20] J. L. Bufton, *A Radiosonde Thermal Sensor Technique for Measurement of Atmospheric Turbulence*, vol. 7867. Washington, DC, USA: National Aeronautics and Space Administration, 1975. [Online]. Available: https://books.google.fr/books?id=78x9ao0cAzUC

[21] R. Hufnagel, "Propagation through atmospheric turbulence," in *The Infrared Handbook*. USA: IRIA Center, Environmental Research Institute of Michigan, 1974, ch. 6. [Online]. Available: https://books.google.fr/books?hl=fr&lr=&id=MwKMUP3NAUsC

[22] P. Ulrich, "Hufnagel-Valley profiles for specified values of the coherence length and isoplanatic angle," WJ Schafer Associates, Arlington, VA, USA, Tech. Rep. MA-TN-88-013, 1988.

[23] G. C. Valley, "Isoplanatic degradation of tilt correction and short-term imaging systems," *Appl. Opt.*, vol. 19, no. 4, pp. 574–577, 1980.

[24] L. C. Andrews, R. L. Phillips, D. Wayne, T. Leclerc, P. Sauer, R. Crabbs, and J. Kiriazes, "Near-ground vertical profile of refractive-index fluctuations," *Proc. SPIE*, vol. 7324, pp. 11–22, May 2009.

[25] *Propagation Data Required for the Design of Earth-Space Systems Operating Between 20 THz and 375 THz*, document ITU-R P.1621-2, 2015.

[26] F. Quatresooz, D. Vanhoenacker-Janvier, and C. Oestges, "Computation of optical refractive index structure parameter from its statistical definition using radiosonde data," *Radio Sci.*, vol. 58, no. 1, pp. 1–16, Jan. 2023.

[27] J. W. Hardy, *Adaptive Optics for Astronomical Telescopes*, vol. 16. New York, NY, USA: Oxford Optical and Imaging Sci., 1998. [Online]. Available: https://books.google.fr/books?id=-0aAWyckS_8C

[28] L. C. Roberts and L. W. Bradford, "Improved models of upper-level wind for several astronomical observatories," *Opt. Exp.*, vol. 19, no. 2, pp. 820–837, 2011.

[29] A. K. Majumdar and J. C. Ricklin, *Free-Space Laser Communications: Principles and Advances*, vol. 2. Berlin, Germany: Springer, 2010.

[30] D. Giggenbach, "Optimierung der optischen freiraumkommunikation durch die turbulente atmosphare-focal array receiver," Ph.D. thesis, Shaker-Verlag, Oberpfaffenhofen, Germany, 2005. [Online]. Available: https://elib.dlr.de/7610/

[31] R. M. Calvo, P. Becker, D. Giggenbach, F. Moll, M. Schwarzer, M. Hinz, and Z. Sodnik, "Transmitter diversity verification on Artemis geostationary satellite," *Proc. SPIE*, vol. 8971, pp. 24–37, Mar. 2014.

[32] R. K. Tyson, "Adaptive optics and ground-to-space laser communications," *Appl. Opt.*, vol. 35, no. 19, pp. 3640–3646, 1996.

[33] L. C. Andrews, R. L. Phillips, D. Wayne, P. Sauer, T. Leclerc, and R. Crabbs, "Creating a C_n^2 profile as a function of altitude using scintillation measurements along a slant path," *Proc. SPIE*, vol. 8238, pp. 95–106, Feb. 2012.

[34] L. C. Andrews, *Field Guide to Atmospheric Optics*, 2nd ed., Washington, DC, USA: SPIE, 2019.

[35] L. B. Stotts and L. C. Andrews, "Adaptive optics model characterizing turbulence mitigation for free space optical communications link budgets," *Opt. Exp.*, vol. 29, no. 13, pp. 20307–20321, 2021.

[36] D. Sadot, "Forecasting optical turbulence strength on the basis of macroscale meteorology and aerosols: Models and validation," *Opt. Eng.*, vol. 31, no. 2, pp. 200–212, 1992.

[37] L. B. Stotts and L. C. Andrews, "Improving the Hufnagel–Andrews–Phillips refractive index structure parameter model using turbulent intensity," *Opt. Exp.*, vol. 31, no. 9, pp. 14265–14277, 2023.

[38] D. A. Mahmood, S. S. Naif, M. H. Al-Jiboori, and T. Al-Rbayee, "Improving Hufnagel–Andrews–Phillips model for prediction C_n^2 using empirical wind speed profiles," *J. Atmos. Solar-Terr. Phys.*, vol. 240, Nov. 2022, Art. no. 105952.

[39] T. Cherubini and S. Businger, "Another look at the refractive index structure function," *J. Appl. Meteorol. Climatol.*, vol. 52, no. 2, pp. 498–506, Feb. 2013.

[40] T. E. VanZandt, J. L. Green, K. S. Gage, and W. L. Clark, "Vertical profiles of refractivity turbulence structure constant: Comparison of observations by the sunset radar with a new theoretical model," *Radio Sci.*, vol. 13, no. 5, pp. 819–829, Sep. 1978.

[41] A. D. Wheelon, *Electromagnetic Scintillation: Volume 1, Geometrical Optics*. Cambridge, U.K.: Cambridge Univ. Press, 2001.

[42] E. L. Andreas, "Estimating C_n^2 over snow and sea ice from meteorological data," *J. Opt. Soc. Amer. A, Opt. Image Sci.*, vol. 5, no. 4, pp. 481–495, 1988.

[43] J. C. Owens, "Optical refractive index of air: Dependence on pressure, temperature and composition," *Appl. Opt.*, vol. 6, no. 1, pp. 51–59, 1967.

[44] R. J. Hill and R. S. Lawrence, "Refractive index of water vapor in infrared windows," *Infr. Phys.*, vol. 26, no. 6, pp. 371–376, Nov. 1986.
[45] B. R. Bean and E. J. Dutton, *Radio Meteorology*, vol. 92. Superintendentof Documents, U.S. Government Print Office, 1966. [Online]. Available: https://books.google.fr/books?id=Jw9RAAAAMAAJ
[46] E. Smith and S. Weintraub, "The constants in the equation for atmospheric refractive index at radio frequencies," *Proc. IRE*, vol. 41, no. 8, pp. 1035–1037, Aug. 1953.
[47] *The Radio Refractive Index: Its Formula and Refractivity Data*, document ITU-R P.453-14, 2019.
[48] A. Ishimaru, *Wave Propagation and Scattering in Random Media*, vol. 2. New York, NY, USA: Academic Press, 1978.
[49] T. Foken and C. J. Napo, *Micrometeorology*, vol. 2. Berlin, Germany: Springer, 2008.
[50] M. Xu, S. Shao, N. Weng, and Q. Liu, "Analysis of the optical turbulence model using meteorological data," *Remote Sens.*, vol. 14, no. 13, p. 3085, Jun. 2022.
[51] S. Wu, C. Su, X. Wu, T. Luo, and X. Li, "A simple method to estimate the refractive index structure parameter (C_n^2) in the atmosphere," *Publications Astronomical Soc. Pacific*, vol. 132, no. 1014, Aug. 2020, Art. no. 084501.
[52] S. Businger, R. McLaren, R. Ogasawara, D. Simons, and R. J. Wainscoat, "Starcasting," *Bull. Amer. Meteorological Soc.*, vol. 83, no. 6, pp. 858–871, Jun. 2002.
[53] C. Qing, X. Wu, X. Li, T. Luo, C. Su, and W. Zhu, "Mesoscale optical turbulence simulations above Tibetan Plateau: First attempt," *Opt. Exp.*, vol. 28, no. 4, pp. 4571–4586, 2020.
[54] G. Y. Jumper, E. A. Murphy, F. H. Ruggiero, J. R. Roadcap, A. J. Ratkowski, J. Vernin, and H. Trinquet, "OHP–APT 2002 gravity wave campaign: Waves, turbulence and forecasts," *Environ. Fluid Mech.*, vol. 7, no. 5, pp. 351–370, Oct. 2007.
[55] P. A. Frederickson, "Integrating atmospheric optical turbulence and numerical weather prediction models for laser performance predictions," *Proc. SPIE*, vol. 11133, pp. 145–152, Sep. 2019.
[56] E. M. Dewan, *A Model for C_n^2 (Optical Turbulence) Profiles Using Radiosonde Data*. MA, USA: Directorate of Geophysics, Air Force Materiel Command, 1993. [Online]. Available: https://books.google.fr/books?id=zngiAQAAIAAJ
[57] R. B. Stull, *An Introduction to Boundary Layer Meteorology*, vol. 13. Berlin, Germany: Springer, 1988.
[58] E. M. Dewan and N. Grossbard, "The inertial range 'outer scale' and optical turbulence," *Environ. Fluid Mech.*, vol. 7, no. 5, pp. 383–396, Oct. 2007.
[59] A. Y. Shikhovtsev, C. Qing, E. A. Kopylov, S. A. Potanin, and P. G. Kovadlo, "Vertical distribution of optical turbulence at the peak terskol observatory and mount kurapdag," *Remote Sens.*, vol. 16, no. 12, p. 2102, Jun. 2024.
[60] A. Jackson, "Modified-dewan optical turbulence parameterizations, air force research laboratory technical report," Air Force Res. Lab., Hanscom AFB, MA, USA, Tech. Rep. AFRL-VS-HA-TR-2004-1116, 2004.
[61] F. H. Ruggiero and D. A. DeBenedictis, "Forecasting optical turbulence from mesoscale numerical weather prediction models," in *Proc. DoD High Perform. Modernization Program Users Group Conf.*, 2002, pp. 10–14.
[62] X. Hu, X. Wu, Q. Yang, Y. Guo, Z. Wang, C. Yan, Z. Qiao, C. Qing, X. Li, and X. Qian, "Effect of data spatial vertical resolution on the estimation of vertical profiles of the refractive index structure constant," *Opt. Exp.*, vol. 31, no. 16, pp. 25815–25828, 2023.
[63] R. R. Beland and J. H. Brown, "A deterministic temperature model for stratospheric optical turbulence," *Phys. Scripta*, vol. 37, no. 3, pp. 419–423, Mar. 1988.
[64] C. E. Coulman, J. Vernin, Y. Coqueugniot, and J. L. Caccia, "Outer scale of turbulence appropriate to modeling refractive-index structure profiles," *Appl. Opt.*, vol. 27, no. 1, pp. 155–160, 1988.
[65] V. P. Lukin, "Outer scale of atmospheric turbulence," *Proc. SPIE*, vol. 5981, Oct. 2005, Art. no. 598101.
[66] L. Montoya, J. De La Rosa, J. Castro-Almazán, I. Montilla, and M. Collados, "Modeling day time turbulence profiles: Application to Teide observatory," in *Adaptive Optics for Extremely Large Telescopes*, 2017.
[67] D. L. Fried, "Optical heterodyne detection of an atmospherically distorted signal wave front," *Proc. IEEE*, vol. 55, no. 1, pp. 57–77, Jan. 1967.
[68] A. Abahamid, A. Jabiri, J. Vernin, Z. Benkhaldoun, M. Azouit, and A. Agabi, "Optical turbulence modeling in the boundary layer and free atmosphere using instrumented meteorological balloons," *Astron. Astrophys.*, vol. 416, no. 3, pp. 1193–1200, Mar. 2004.
[69] J. Warnock, T. VanZandt, and J. Green, "A statistical model to estimate mean values of parameters of turbulence in the free atmosphere," in *Proc. Symp. Turbulence Diffusion*, Boulder, CO, USA, 1985, pp. 156–159.
[70] G. d'Auria, F. S. Marzano, and U. Merlo, "Model for estimating the refractive-index structure constant in clear-air intermittent turbulence," *Appl. Opt.*, vol. 32, no. 15, pp. 2674–2680, 1993.
[71] H. Vasseur, "Prediction of tropospheric scintillation on satellite links from radiosonde data," *IEEE Trans. Antennas Propag.*, vol. 47, no. 2, pp. 293–301, Feb. 1999.
[72] J. Warnock and T. Vanzandt, "Statistical model to estimate the refractivity turbulence structure constant C_n^2 in the free atmosphere," *NOAA Tech. Memorandum ERL AL-10*, 1985.
[73] S. Basu, A. W. DeMarco, and P. He, "On the dissipation rate of temperature fluctuations in stably stratified flows," *Environ. Fluid Mech.*, vol. 21, no. 1, pp. 63–82, Feb. 2021.
[74] R. V. Ozmidov, "Vertical exchange in the ocean," *Phys. Oceanogr.*, vol. 9, no. 6, pp. 417–425, Nov. 1999.
[75] S. Corrsin, *Local Isotropy in Turbulent Shear Flow*. Washington, DC, USA: National Advisory Committee for Aeronautics, 1958. [Online]. Available: https://ntrs.nasa.gov/api/citations/19930089981/downloads/19930089981.pdf
[76] N. M. Gavrilov, H. Luce, M. Crochet, F. Dalaudier, and S. Fukao, "Turbulence parameter estimations from high-resolution balloon temperature measurements of the MUTSI-2000 campaign," in *Annales Geophysicae*. Göttingen, Germany: Copernicus, 2005.
[77] C. A. Clayson and L. Kantha, "On turbulence and mixing in the free atmosphere inferred from high-resolution soundings," *J. Atmos. Ocean. Technol.*, vol. 25, no. 6, pp. 833–852, Jun. 2008.
[78] S. A. Thorpe, "Turbulence and mixing in a Scottish loch," *Phil. Trans. Roy. Soc. London. Ser. A, Math. Phys. Sci.*, vol. 286, no. 1334, pp. 125–181, 1977.
[79] E. Martini, A. Freni, F. Cuccoli, and L. Facheris, "Derivation of clear-air turbulence parameters from high-resolution radiosonde data," *J. Atmos. Ocean. Technol.*, vol. 34, no. 2, pp. 277–293, Feb. 2017.
[80] H. Zhang, L. Zhu, G. Sun, K. Zhang, Y. Liu, X. Ma, H. Zhang, Q. Liu, S. Cui, T. Luo, X. Li, and N. Weng, "A multi-model ensemble pattern method to estimate the refractive index structure parameter profile and integrated astronomical parameters in the atmosphere," *Remote Sens.*, vol. 15, no. 6, p. 1584, Mar. 2023.
[81] S. Basu, "A simple approach for estimating the refractive index structure parameter (C_n^2) profile in the atmosphere," *Opt. Lett.*, vol. 40, no. 17, pp. 4130–4133, 2015.
[82] D. Nath, M. V. Ratnam, A. K. Patra, B. V. K. Murthy, and S. V. B. Rao, "Turbulence characteristics over tropical station gadanki (13.5 °N, 79.2 °E) estimated using high-resolution GPS radiosonde data," *J. Geophys. Res., Atmos.*, vol. 115, no. D7, Apr. 2010. [Online]. Available: https://agupubs.onlinelibrary.wiley.com/doi/full/10.1029/2009JD012347
[83] X. Hu, X. Wu, Q. Yang, Y. Guo, Z. Wang, C. Qing, X. Li, and X. Qian, "Estimation and characterization of atmospheric turbulence in the free atmosphere above the Tibetan Plateau using the Thorpe method," *Appl. Opt.*, vol. 62, no. 4, pp. 1115–1122, 2023.
[84] R. Wilson, F. Dalaudier, and H. Luce, "Can one detect small-scale turbulence from standard meteorological radiosondes?" *Atmos. Meas. Techn.*, vol. 4, no. 5, pp. 795–804, May 2011.
[85] T. H. Ellison, "Turbulent transport of heat and momentum from an infinite rough plane," *J. Fluid Mech.*, vol. 2, no. 5, pp. 456–466, Jul. 1957.
[86] E. Masciadri, J. Vernin, and P. Bougeault, "3D mapping of optical turbulence using an atmospheric numerical model: I. A useful tool for the ground-based astronomy," *Astron. Astrophys. Suppl. Ser.*, vol. 137, no. 1, pp. 185–202, May 1999.
[87] J. W. Deardorff, "Stratocumulus-capped mixed layers derived from a three-dimensional model," *Boundary-Layer Meteorol.*, vol. 18, no. 4, pp. 495–527, Jun. 1980.
[88] M. Tjernström, "Turbulence length scales in stably stratified free shear flow analyzed from slant aircraft profiles," *J. Appl. Meteorol.*, vol. 32, no. 5, pp. 948–963, May 1993.
[89] J. F. Louis, "A short history of the operational PBL parameterization at ECMWF," in *Proc. Workshop Planet. Boundary Layer Parameterization*, 1982.
[90] D. Sprung, C. Ullwer, A. M. van Eijk, and K. Stein, "Investigation of vertical profiles of optical turbulence from mesoscale simulations runs and radiosonde data," *Proc. SPIE*, vol. 11860, pp. 11–19, Sep. 2021.
[91] C. Ullwer, D. Sprung, K. Stein, and A. van Eijk, "Sensitivity study on the number of height levels used in a numerical weather model to determine the vertical profile of C_n^2," *Proc. SPIE*, vol. 12731, pp. 178–184, Oct. 2023.

[92] A. Rafalimanana, C. Giordano, A. Ziad, and E. Aristidi, "Optimal prediction of atmospheric turbulence by means of the weather research and forecasting model," *Publications Astronomical Soc. Pacific*, vol. 134, no. 1035, May 2022, Art. no. 055002.
[93] V. Tatarski, *Wave Propagation in a Turbulent Medium*. New York, NY, USA: McGraw-Hill, 1961.
[94] S. Wu, X. Wu, C. Su, Q. Yang, J. Xu, T. Luo, C. Huang, and C. Qing, "Reliable model to estimate the profile of the refractive index structure parameter (C_n^2) and integrated astroclimatic parameters in the atmosphere," *Opt. Exp.*, vol. 29, no. 8, pp. 12454–12470, 2021.
[95] H. Trinquet and J. Vernin, "A statistical model to forecast the profile of the index structure constant," *Environ. Fluid Mech.*, vol. 7, no. 5, pp. 397–407, 2007.
[96] C. Giordano, A. Rafalimanana, A. Ziad, E. Aristidi, J. Chabé, Y. Fanteï-Caujole, and C. Renaud, "Contribution of statistical site learning to improve optical turbulence forecasting," *Monthly Notices Roy. Astronomical Soc.*, vol. 504, no. 2, pp. 1927–1938, Apr. 2021.
[97] C. Giordano, J. Vernin, H. Trinquet, and C. Muñoz-Tuñón, "Weather research and forecasting prevision model as a tool to search for the best sites for astronomy: Application to La Palma, Canary Islands," *Monthly Notices Roy. Astronomical Soc.*, vol. 440, no. 3, pp. 1964–1970, Apr. 2014.
[98] X. Qian, Y. Yao, L. Zou, H. Wang, J. Yin, and Y. Li, "Modelling of atmospheric optical turbulence with the Weather Research and Forecasting model at the Ali observatory, Tibet," *Monthly Notices Roy. Astronomical Soc.*, vol. 505, no. 1, pp. 582–592, Dec. 2021.
[99] D. Walters and K. Kunkel, "Atmospheric modulation transfer function for desert and mountain locations: The atmospheric effects on r_0," *J. Opt. Soc. Amer.*, vol. 71, no. 4, pp. 397–405, 1981.
[100] C. Qing, X. Wu, H. Huang, Q. Tian, W. Zhu, R. Rao, and X. Li, "Estimating the surface layer refractive index structure constant over snow and sea ice using Monin-Obukhov similarity theory with a mesoscale atmospheric model," *Opt. Exp.*, vol. 24, no. 18, pp. 20424–20436, 2016.
[101] C. Ullwer, D. Sprung, E. Sucher, T. Kociok, P. Großmann, A. M. J. V. Eijk, and K. Stein, "Global simulations of C_n^2 using the weather research and forecast model WRF and comparison to experimental results," *Proc. SPIE*, vol. 11133, pp. 126–136, Sep. 2019.
[102] J. Gottlieb and N. S. Kopeika, "Prediction of coarse-aerosol statistics according to weather forecast," *Proc. SPIE*, vol. 1487, pp. 184–191, Jul. 1991.
[103] D. Sadot, "Prediction of overall atmospheric modulation transfer function with standard weather parameters: Comparison with measurements with two imaging systems," *Opt. Eng.*, vol. 34, no. 11, pp. 3239–3248, Nov. 1995.
[104] Y. Yitzhaky, "Restoration of atmospherically blurred images according to weather-predicted atmospheric modulation transfer functions," *Opt. Eng.*, vol. 36, no. 11, pp. 3064–3072, Nov. 1997.
[105] R. Barrios and F. Dios, "Wireless optical communications through the turbulent atmosphere: A review," in *Optical Communications Systems*, Mar. 2012, ch. 1, pp. 1–40. [Online]. Available: https://books.google.fr/books?id=hnCPDwAAQBAJ
[106] L. Hudcova and O. Wilfert, "Prediction of atmospheric turbulence on the basis of weather conditions," in *Proc. Conf. Microw. Techn. (COMITE)*, Apr. 2017, pp. 1–5.
[107] T. T. Leclerc, R. L. Phillips, L. C. Andrews, D. T. Wayne, P. Sauer, and R. Crabbs, "Prediction of the ground-level refractive index structure parameter from the measurement of atmospheric conditions," *Proc. SPIE*, vol. 7685, pp. 74–81, Apr. 2010.
[108] S. Bendersky, N. S. Kopeika, and N. Blaunstein, "Atmospheric optical turbulence over land in middle east coastal environments: Prediction modeling and measurements," *Appl. Opt.*, vol. 43, no. 20, pp. 4070–4079, 2004.
[109] E. Ryznar and J. Bartlo, "Dependence of C_n^2 C_T^2 in the atmospheric boundary layer on conventional meteorological variables," College Eng., Dept. Atmos. Ocean. Sci., Univ. Michigan, Ann Arbor, MI, USA, Tech. Rep. AFGL-TR-86-0013, 1985, pp. 2143–48109.
[110] T. S. Carvalho, C. P. Azzolin, A. F. Gurgel, V. G. A. Carneiro, and M. T. M. R. Giraldi, "Statistical modeling of atmospheric turbulence based on a low-cost experimental setup for measuring C_n^2 over water," *J. Opt. Soc. Amer. A, Opt. Image Sci.*, vol. 40, no. 4, pp. 101–107, 2023.
[111] H. Wang, B. Li, X. Wu, C. Liu, Z. Hu, and P. Xu, "Prediction model of atmospheric refractive index structure parameter in coastal area," *J. Modern Opt.*, vol. 62, no. 16, pp. 1336–1346, Sep. 2015.
[112] A. A. B. Raj, J. A. V. Selvi, and S. Durairaj, "Comparison of different models for ground-level atmospheric turbulence strength (C_n^2) prediction with a new model according to local weather data for FSO applications," *Appl. Opt.*, vol. 54, no. 4, pp. 802–815, 2015.
[113] J. C. Wyngaard, Y. Izumi, and S. A. Collins, "Behavior of the refractive-index-structure parameter near the ground," *J. Opt. Soc. Amer.*, vol. 61, no. 12, pp. 1646–1650, Dec. 1971.
[114] P. A. Frederickson, K. L. Davidson, C. R. Zeisse, and C. S. Bendall, "Estimating the refractive index structure parameter C_n^2 over the ocean using bulk methods," *J. Appl. Meteorol.*, vol. 39, no. 10, pp. 1770–1783, Oct. 2000.
[115] K. L. Davidson, G. E. Schacher, C. W. Fairall, and A. K. Goroch, "Verification of the bulk method for calculating overwater optical turbulence," *Appl. Opt.*, vol. 20, no. 17, pp. 2919–2924, 1981.
[116] J. C. Wyngaard, *Turbulence in the Atmosphere*. Cambridge, U.K.: Cambridge Univ. Press, 2010.
[117] T. Foken, "50 years of the Monin–Obukhov similarity theory," *Boundary-Layer Meteorol.*, vol. 119, no. 3, pp. 431–447, Jun. 2006.
[118] H. A. Panofsky, "Determination of stress from wind and temperature measurements," *Quart. J. Roy. Meteorological Soc.*, vol. 89, no. 379, pp. 85–94, Jan. 1963.
[119] C. A. Paulson, "The mathematical representation of wind speed and temperature profiles in the unstable atmospheric surface layer," *J. Appl. Meteorol.*, vol. 9, no. 6, pp. 857–861, Dec. 1970.
[120] E. L. Andreas and A. P. Makshtas, "Energy exchange over Antarctic sea ice in the spring," *J. Geophys. Res., Oceans*, vol. 90, no. 4, pp. 7199–7212, Jul. 1985.
[121] C. Qing, X. Wu, X. Li, W. Zhu, C. Qiao, R. Rao, and H. Mei, "Use of weather research and forecasting model outputs to obtain near-surface refractive index structure constant over the ocean," *Opt. Exp.*, vol. 24, no. 12, pp. 13303–13315, 2016.
[122] G. J. Kunz, "A bulk model to predict optical turbulence in the marine surface layer," The Hague, The Netherlands, Tech. Rep. TNO, FEL-96-A053, 1996.
[123] C. A. Friehe, "Estimation of the refractive-index temperature structure parameter over the ocean," *Appl. Opt.*, vol. 16, no. 2, pp. 334–340, 1977.
[124] C. Qing, X. Wu, X. Li, Q. Tian, D. Liu, R. Rao, and W. Zhu, "Simulating the refractive index structure constant in the surface layer at Antarctica with a mesoscale model," *Astronomical J.*, vol. 155, no. 1, p. 37, 2017.
[125] C. Qing, X. Wu, X. Li, and W. Zhu, "Performance analysis of weather research and forecasting model for simulating near-surface optical turbulence over land," *Optik*, vol. 188, pp. 225–232, Jul. 2019.
[126] A. Tunick, "CN_2 model to calculate the micrometeorological influences on the refractive index structure parameter," *Environ. Model. Softw.*, vol. 18, no. 2, pp. 165–171, Mar. 2003.
[127] H. Rachele, A. Tunick, and F. V. Hansen, "MARIAH—A similarity-based method for determining wind, temperature, and humidity profile structure in the atmospheric surface layer," *J. Appl. Meteorol.*, vol. 34, no. 4, pp. 1000–1005, Apr. 1995.
[128] V. Thiermann and H. Grassl, "The measurement of turbulent surface-layer fluxes by use of bichromatic scintillation," *Boundary-Layer Meteorol.*, vol. 58, no. 4, pp. 367–389, Mar. 1992.
[129] V. Thiermann and A. Kohnle, "A simple model for the structure constant of temperature fluctuations in the lower atmosphere," *J. Phys. D, Appl. Phys.*, vol. 21, no. 10S, pp. 37–40, Oct. 1988.
[130] S. Doss-Hammel, E. Oh, J. C. Ricklin, F. D. Eaton, G. C. Gilbreath, and D. Tsintikidis, "A comparison of optical turbulence models," *Proc. SPIE*, vol. 5550, pp. 236–246, Oct. 2004.
[131] E. Oh, J. C. Ricklin, G. C. Gilbreath, N. J. Vallestero, and F. D. Eaton, "Optical turbulence model for laser propagation and imaging applications," *Proc. SPIE*, vol. 5160, pp. 25–32, Jan. 2004.
[132] Y. H. Oh, J. C. Ricklin, E. Oh, S. Doss-Hammel, and F. D. Eaton, "Estimating optical turbulence effects on free-space laser communication: Modeling and measurements at ARL's ALOT facility," *Proc. SPIE*, vol. 5550, pp. 247–255, Oct. 2004.
[133] K. E. Kunkel and D. L. Walters, "Modeling the diurnal dependence of the optical refractive index structure parameter," *J. Geophys. Res., Oceans*, vol. 88, no. 15, pp. 10999–11004, Dec. 1983.
[134] R. Mahon, C. I. Moore, M. S. Ferraro, W. S. Rabinovich, and P. A. Frederickson, "Comparison of maritime measurements of C_n^2 with NAVSLaM model predictions," *Appl. Opt.*, vol. 59, no. 33, pp. 10599–10612, 2020.
[135] S. Barnett, J. Blau, P. Frederickson, and K. Cohn, "Measurements and modeling of optical turbulence in the coastal environment," *Appl. Sci.*, vol. 12, no. 10, p. 4892, May 2022.

[136] S. Cheinet, A. Beljaars, K. Weiss-Wrana, and Y. Hurtaud, "The use of weather forecasts to characterise near-surface optical turbulence," *Boundary-Layer Meteorol.*, vol. 138, no. 3, pp. 453–473, Mar. 2011.
[137] F. Quatresooz, R. Griffiths, L. Bardou, R. Wilson, J. Osborn, D. Vanhoenacker-Janvier, and C. Oestges, "Continuous daytime and nighttime forecast of atmospheric optical turbulence from numerical weather prediction models," *Opt. Exp.*, vol. 31, no. 21, pp. 33850–33872, 2023.
[138] J. C. Kaimal, J. C. Wyngaard, D. A. Haugen, O. R. Coté, Y. Izumi, S. J. Caughey, and C. J. Readings, "Turbulence structure in the convective boundary layer," *J. Atmos. Sci.*, vol. 33, no. 11, pp. 2152–2169, Nov. 1976.
[139] V. Kukharets and L. Tsvang, "Structure parameter of the refractive index in the atmospheric boundary layer," *Acad. Sci., USSR, Izvestiya, Atmos. Ocean. Phys.*, vol. 16, pp. 73–77, Jan. 1980.
[140] E. A. Murphy, E. M. Dewan, and S. M. Sheldon, "Daytime comparisons of C_n^2 models to measurements in a desert location," *Proc. SPIE*, vol. 551, pp. 156–162, Jan. 1986.
[141] K. E. Kunkel, D. L. Walters, and G. A. Ely, "Behavior of the temperature structure parameter in a desert basin," *J. Appl. Meteorol.*, vol. 20, no. 2, pp. 130–136, Feb. 1981.
[142] J. C. Kaimal and J. J. Finnigan, *Atmospheric Boundary Layer Flows: Their Structure and Measurement*. Oxford, U.K.: Oxford Univ. Press, 1994.
[143] Y. Wang and S. Basu, "Using an artificial neural network approach to estimate surface-layer optical turbulence at Mauna Loa, Hawaii," *Opt. Lett.*, vol. 41, no. 10, pp. 2334–2337, 2016.
[144] C. Su, X. Wu, T. Luo, S. Wu, and C. Qing, "Adaptive niche-genetic algorithm based on backpropagation neural network for atmospheric turbulence forecasting," *Appl. Opt.*, vol. 59, no. 12, pp. 3699–3705, 2020.
[145] T. Butterleya, J. Osborna, M. Sarazinb, and R. Wilsona, "Nowcasting of the surface layer of turbulence at paranal observatory," in *Proc. AO4ELT5*. Tenerife, Spain: Canary Islands, 2017.
[146] J. J. Rudiger, K. Book, J. S. de Grassie, S. Hammel, and B. Baker, "A machine learning approach for forecasting the refractive index structure parameter," *Proc. SPIE*, vol. 10770, pp. 187–195, Nov. 2018.
[147] A. Lionis, G. Chaskakis, K. Cohn, J. Blau, K. Peppas, H. E. Nistazakis, and A. Tsigopoulos, "Optical turbulence measurements and modeling over Monterey Bay," *Opt. Commun.*, vol. 520, Oct. 2022, Art. no. 128508.
[148] A. Lionis, K. Peppas, H. E. Nistazakis, A. Tsigopoulos, K. Cohn, and K. R. Drexler, "Supervised machine learning for refractive index structure parameter modeling," *Quantum Beam Sci.*, vol. 7, no. 2, p. 18, Jun. 2023.
[149] B. N. Campbell, K. McBryde, E. Walter, and K. Drexler, "Machine learning for optical turbulence prediction in geographically similar regions," *Proc. SPIE*, vol. 12691, pp. 215–223, Aug. 2023.
[150] A. Sklavounos, "Measurements of optical turbulence and analysis using machine learning," M.S. thesis, Naval Postgraduate School, Monterey, CA, USA, 2021.
[151] C. Jellen, J. Burkhardt, C. Brownell, and C. Nelson, "Machine learning informed predictor importance measures of environmental parameters in maritime optical turbulence," *Appl. Opt.*, vol. 59, no. 21, pp. 6379–6389, 2020.
[152] C. Jellen, M. Oakley, C. Nelson, J. Burkhardt, and C. Brownell, "Machine-learning informed macro-meteorological models for the near-maritime environment," *Appl. Opt.*, vol. 60, no. 11, pp. 2938–2951, 2021.
[153] L. A. Bolbasova, A. A. Andrakhanov, and A. Y. Shikhovtsev, "The application of machine learning to predictions of optical turbulence in the surface layer at Baikal astrophysical observatory," *Monthly Notices Roy. Astronomical Soc.*, vol. 504, no. 4, pp. 6008–6017, May 2021.
[154] C. Jellen, C. Nelson, J. Burkhardt, and C. Brownell, "Hybrid optical turbulence models using machine-learning and local measurements," *Appl. Opt.*, vol. 62, no. 18, pp. 4880–4890, 2023.
[155] C. Su, X. Wu, S. Wu, Q. Yang, Y. Han, C. Qing, T. Luo, and Y. Liu, "In situ measurements and neural network analysis of the profiles of optical turbulence over the Tibetan Plateau," *Monthly Notices Roy. Astronomical Soc.*, vol. 506, no. 2, pp. 3430–3438, Jul. 2021.
[156] C. Bi, C. Qing, P. Wu, X. Jin, Q. Liu, X. Qian, W. Zhu, and N. Weng, "Optical turbulence profile in marine environment with artificial neural network model," *Remote Sens.*, vol. 14, no. 9, p. 2267, May 2022.
[157] M. Xu, S. Shao, Q. Liu, G. Sun, Y. Han, and N. Weng, "Optical turbulence profile forecasting and verification in the offshore atmospheric boundary layer," *Appl. Sci.*, vol. 11, no. 18, p. 8523, Sep. 2021.
[158] M. Pierzyna, R. Saathof, and S. Basu, "Π-ML: A dimensional analysis-based machine learning parameterization of optical turbulence in the atmospheric surface layer," *Opt. Lett.*, vol. 48, no. 17, pp. 4484–4487, Jul. 2023.
[159] J. Vernin, "Mechanism of formation of optical turbulence (invited speaker)," in *Proc. Astronomical Site Eval. Visible Radio Range*, vol. 266, Jan. 2002, p. 2.
[160] N. Védrenne, C. Petit, A. Montmerle-Bonnefois, C. B. Lim, J.-M. Conan, L. Paillier, K. Caillault, F. Gustave, A. Durécu, V. Michau, F. Cassaing, S. Meimon, and J. Montri, "Performance analysis of an adaptive optics based optical feeder link ground station," *Proc. SPIE*, vol. 11852, pp. 527–535, Jun. 2021.
[161] F. Quatresooz, D. Vanhoenacker-Janvier, and C. Oestges, "Daytime forecast of optical turbulence for optical communications," in *Proc. Commun. Observ. Through Atmos. Turbulence (COAT) Workshop*, Mar. 2023. [Online]. Available: https://hal.science/hal-04605062/
[162] A. Rafalimanana, C. Giordano, A. Ziad, and E. Aristidi, "Toward an optimal prediction of atmospheric turbulence by means of WRF model," *Proc. SPIE*, vol. 11448, pp. 1524–1534, Dec. 2020.
[163] E. Masciadri, F. Lascaux, and L. Fini, "MOSE: Operational forecast of the optical turbulence and atmospheric parameters at European southern observatory ground-based sites—I. Overview and vertical stratification of atmospheric parameters at 0–20 km," *Monthly Notices Roy. Astronomical Soc.*, vol. 436, no. 3, pp. 1968–1985, Dec. 2013.
[164] A. Turchi, E. Masciadri, and L. Fini, "Forecasting surface-layer atmospheric parameters at the large binocular telescope site," *Monthly Notices Roy. Astronomical Soc.*, vol. 466, no. 2, pp. 1925–1943, Aug. 2016.
[165] C. Bi, X. Qian, Q. Liu, W. Zhu, X. Li, T. Luo, X. Wu, and C. Qing, "Estimating and measurement of atmospheric optical turbulence according to balloon-borne radiosonde for three sites in China," *J. Opt. Soc. Amer. A, Opt. Image Sci.*, vol. 37, no. 11, pp. 1785–1794, 2020.
[166] F. Lascaux, E. Masciadri, and L. Fini, "Forecast of surface layer meteorological parameters at cerro paranal with a mesoscale atmospherical model," *Monthly Notices Roy. Astronomical Soc.*, vol. 449, no. 2, pp. 1664–1678, Mar. 2015.
[167] C. J. Willmott, S. M. Robeson, and K. Matsuura, "A refined index of model performance," *Int. J. Climatol.*, vol. 32, no. 13, pp. 2088–2094, Nov. 2012.

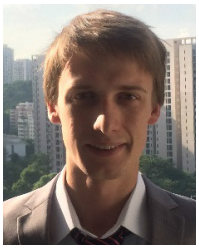

FLORIAN QUATRESOOZ received the B.Sc. and M.Sc. degrees in electrical engineering from Université catholique de Louvain (UCLouvain), Louvain-la-Neuve, Belgium, in 2018 and 2020, respectively, and the Ph.D. degree from the Institute for Information and Communication Technologies, Electronics, and Applied Mathematics (ICTEAM), UCLouvain, in 2024. His research interests include electromagnetic wave propagation and atmospheric modeling for free-space optical communications.

CLAUDE OESTGES (Fellow, IEEE) received the M.Sc. and Ph.D. degrees in electrical engineering from the Université catholique de Louvain (UCLouvain), Louvain-la-Neuve, Belgium, in 1996 and 2000, respectively. In January 2001, he joined as a Postdoctoral Scholar with the Smart Antennas Research Group (Information Systems Laboratory), Stanford University, CA, USA. From January 2002 to September 2005, he was associated with the Microwave Laboratory, UCLouvain, as a Postdoctoral Fellow with the Belgian Fonds de la Recherche Scientifique (FRS-FNRS). He is currently a Full Professor with the Electrical Engineering Department, Institute for Information and Communication Technologies, Electronics and Applied Mathematics (ICTEAM), UCLouvain. He is the author or co-author of four books and more than 200 journal articles and conference communications. He was a recipient of the 1999–2000 IET Marconi Premium Award and the IEEE Vehicular Technology Society Neal Shepherd Award, in 2004 and 2012, respectively, and the EurAAP Propagation Award, in 2024. He was the Chair of COST Action CA15104 IRACON, from 2016 to 2020.